Surface & Coatings Technology 375 (2019) 652–669

Contents lists available at ScienceDirect

Surface & Coatings Technology

journal homepage: www.elsevier.com/locate/surfcoat

$LaCl_3$-modified Ni deposits on 3D-heterotypic porous Ti surface for strengthening its mechanical and electrochemical properties

Xiaowei Zhou*, Yuxin Wang

School of Materials Science and Engineering, Jiangsu University of Science and Technology, Zhenjiang 212003, PR China

ARTICLE INFO

Keywords:
Surface anodizing
Ni-$LaCl_3$ deposits
3D-heterotypic nanopores
Wear

ABSTRACT

For increasing the interfacial bonding of Ni deposits onto Ti surface, the objectives of this work are to explore an effective approach for $LaCl_3$-modified Ni nanocrystals on porous surface of Ti substrate. Three-dimensional (3D) heterotypic nanopores were well organized with a diameter size of ~300 nm through surface anodizing in H_3PO_4-containing acid solution at DC 180 V. In view of the above considerations, the anodized surface with a 3D-open reticular structure was processed of high adsorption capacity leading into pitting growth of Ni crystals into 3D-pores. Experimental data have referred that a leaf-like surface with the diversified orientations of Ni (111) (200) (220) (311) facets were conducted for Ni-$LaCl_3$ deposits instead of an exclusive growth of Ni (111) (200) facets for pure Ni. Based on Nanoindentation tests, it exhibited the ratio of micro hardness (H^3) and elastic modulus (E^2) of Ni samples remarkably increased with increasing $LaCl_3$ addition from 0 to 2.0 g/L. As excepted, the steady-state friction coefficient was ~0.28 for Ni-2.0 g/L $LaCl_3$ composites, which was about one order of magnitude lower than that of pure Ni sample during oxidized at 500 °C in air. The exceptional improvements of corrosion resistance for $LaCl_3$-modified Ni deposits were associated with the co-existence of high adsorptive La^{3+} ions and the La-rich insoluble corrosive products in 1 M (mol/L) HCl solution. In light of this, Ni-based nanocomposites on 3D-heterotypic porous surface of Ti alloys would provide an effective guidance for protecting Ti alloys against wear and corrosive damages.

1. Introduction

Titanium (Ti) and its alloys are emerging as an attractive candidate that have attracted increasing attention as structural materials in various areas of aerospace, catalysis, and biological industries [1–3]. Because of its low density, high strength to weight ratio, superior corrosion resistance and bio-compatibility, Ti alloys have been accepted as one of the most promising candidates to satisfy an increasingly engineering demand for aerospace, marine devices, metallurgical implants, etc. As yet, it commonly existed such predominant intrinsic defects as lower micro hardness, poor wear resistance, and inferior weldability, thus restricting its practical applications [4,5]. In view of this, many progresses have made for surface modification of Ti alloys, for example, mechanical alloying [6], friction stir processing (FSP) [7], physical vapor deposition (PVD) [8], double-glow sputtering technique [9], micro-arc oxidation [10], laser-induced cladding [11], thermal spraying processes [12], etc. Among them, most of current works focused on surface strengthening of Ti alloys using the laser-assisted surface cladding or mechanical alloying, but few studies concerned about bonding interfaces between Ti substrate and its surface coatings. Worse still, the laser-assisted surface film was relatively thin with a low efficiency, hence leading into the failure of coatings' spalling or deformations of Ti substrates [13]. So it was essential for us to develop an excellent anti-wear surface coating with a metallurgical bond towards Ti substrate with superior properties.

Till now, many studies have carried out for surface strengthening of Ti alloys, but few studies focused on Ni-RE composite coatings onto porous Ti surface. The Rare- Earth (RE) additives with specially catalytic and physical properties were expected as a typical of strengthening phase into Ni-, Al-, Co-alloys [14]. Ni-RE coatings, as a promising high-temperature alloy, were the most refractory compounds with a higher melting point (over 2000 °C), comparing to that of pure Ni coatings (~1453 °C). In recent year, Ni-RE composites including Ni-P/CeO_2, Ni-Co-W/Y_2O_3, Ni-La_2O_3, Ti-Nd_2O_3, etc., have been applicable for engineering applications. Among them, Ni-CeO_2 composite coatings have been extensively employed for functional coatings due to its denser structure and superior properties with Ce-rich disperses through aging treatments [15]. Xue et al. [16] demonstrated that both of microhardness and wear resistance was better for Ni-La_2O_3 composites relative to pure Ni samples. In the case of RE-rich Ni composites, the wear rate was

* Corresponding author.
E-mail address: zhouxiaowei901@just.edu.cn (X. Zhou).

https://doi.org/10.1016/j.surfcoat.2019.07.063
Received 15 April 2019; Received in revised form 20 July 2019; Accepted 28 July 2019
Available online 31 July 2019

much lower irrespective of having minimum friction coefficient. From the wear point of view, Ni modified by RE-oxides (CeO_2, La_2O_3, etc.) have been recognized an attractive candidate for next applications in the form of passive films instead of bulk form. According to our previous studies, an effective and one-step way successfully designed for porous Ti surface with electroless Ni−P interlayer, as a result of adherent layers for self-organizing Ni- composites onto porous surface of Ti substrate [17].

Commonly, the bottleneck in surface modifications for Ti alloys was restricted by its barrier layers in the form of TiO_2 or TiO ceramic oxides. The Ti−O oxides that spontaneously formed on Ti surface were processed of ceramic-like phase structure to limit the growth of surface coatings, resulting in poor interfacial strength between Ti substrate and its surface coatings. In view of these, recent studies on surface anodizing using H_3PO_4-containing solution were carried out, showing that the activated surface with porous TiO_2 arrays was finally acted as templates for Ti−Ni gradient deposits with a superior interfacial bonding between Ti and its surface coatings [18]. Few studies about electroplating on the anodized titanium oxide (ATO) porous surface were addressed, still remaining unexplored. To address above troubles, recent survey found that the 3D-heterotypic porous Ti surface was very critical for increasing mechanical properties. Presently, our group [19,20] have assigned that Ti substrate with nanoporous structure was successfully achieved through electrochemical anodizing. In this respect, surface electroplating of Ni-RE($LaCl_3$) composites onto ATO surface was studied, showing great improvements of interfacial bonding for surface coatings on Ti surface. The effectiveness of Ni-based composites with superior wear resistance could be projected.

Great progresses have been made for surface strengthening of titanium alloys, but few studies focused on the Ni-$LaCl_3$ deposits. Unlike RE (Ce)-oxides, the effects of free-stated La^{3+} ions in Ni electroplating bath are rarely explored. In view of this, the objectives of our current research are to develop an efficient approach for surface electroplating of Ni-$LaCl_3$ coatings on a 3D-heterotypic porous Ti surface. Besides the diffusion behaviors of Ni^{2+} ions through ATO pores were reviewed, further explaining an interfacial bonding between Ni coating and Ti substrate. Results indicated the adding of La^{3+} into Watts-Ni bath was in favor of diversified orientations for Ni-$LaCl_3$ deposits instead of exclusively growing for pure Ni, showing refinement effects and structural integrity for the as-deposited Ni coatings with the addition of $LaCl_3$. Alternatively, the wear and corrosive behaviors of Ni coatings without and with $LaCl_3$ addition were compared, and the electrochemical tests were carried out in 1 M HCl aqueous solution, respectively.

2. Experimental details

2.1. Pre-treatments for ATO surface

Commercially pure titanium plate (Pure Grade 2, TA2) with dimensions of 100 mm × 20 mm × 0.6 mm was selected as Ti substrate. Prior to coating's preparation, surface pre-treatments for Ti substrate were successively followed as: mechanical grinding, metallographic polishing, surface anodizing in phosphoric-mixed acid solution, followed by electroless Ni−P and Ni-$LaCl_3$ deposits. Among them, the electrode spacing of anodic oxidation was 3–5 cm. For electrolytic composition of anodizing and its conditions for ATO surface, it was summarized as Table 1. All the chemicals were used as received without further purification. Herein small additives were sodium dodecyl sulfate (SDS), glycerol, etc., acting as dispersants to increase its hydrophilicity of porous surface. Based on our comparative studies, ATO nanoporous surface with a diameter size of ~300 nm was finally achieved, followed by Ni-$LaCl_3$ deposits. More important, an alternating magnetic field (2nT intensity and ~20 Hz frequency) combined with the long-time anodizing processes in 5–10 °C bath (ice-packs) was

Table 1
Composition of anodizing electrolyte for nanoporous ATO surface.

Composition of anodizing solution and its conditions for ATO template	
H_2SO_4 (98 wt%)	200–300 g/L
H_3PO_4 (85 wt%)	30–50 g/L
H_2O_2 (30 wt%)	~15 mL/L
Small additives (e.g. SDS)	~0.5 g/L
Temperature	10–15 °C (ice packs)
Stirring rate	100–200 rpm
Anodizing voltage	150–180 V (DC)
Anodizing time	5–10 min

propitious to a 3D-open reticular structure. The as-formed 3D porous surface was processed of high adsorption capacity resulting in pitting growth of Ni nanocrystals into ATO pores. For a schematic process of the magnetic-assisted anodizing, it was in Fig. 1a. Fig. 1b and c depict FE-SEM observations of surface and the cross-sectional review for 3D-heterotypic ATO pores. Specially, the free-stated La^{3+} ions with a larger ionic radius (0.11 nm vs. 0.07 nm for Ni^{2+}) would make an all-round adsorption towards the ATO porous surface with a 3D-open reticular channel. After chemical activating using Pd−Sn catalysis, the as-anodized Ti template was quickly placed into a Watts-Nickel bath. The basic electrolyte composed of analytical reagents was listed as: 350 g/L Nickel sulfate, 40 g/L nickel chloride, 50 g/L Boric acid, ~2.0 g/L Lanthanum chloride ($LaCl_3{\cdot}7H_2O$), etc. Pure Ni and Ni-$LaCl_3$ coatings were deposited. In order to ensure the stability of electrolytic solution, the bath temperature was maintained 30 ± 2 °C, and its pH value was adjusted to ~3.0 by adding a dilute H_2SO_4 solution.

The Watts-Ni electrolyte with different $LaCl_3{\cdot}7H_2O$ amounts (0–2.0 g/L) were utilized for Ni-$LaCl_3$ composites. For uniform distribution of $LaCl_3$ addition in Ni coatings, the bath was continuously oscillated under mechanical stirring of 100 rpm. According to our preliminary study, the optimized parameters designed for double-pulsed electroplating were processed at 1500 Hz for pulse frequency and a duty cycle of 25% for the On-Off ratio, together with ultrasonic field (80 kHz/100 W). Finally, the Ni-$LaCl_3$ coatings with a thickness of ~15 μm were obtained, and then sampled after predetermined time, followed by air cooling.

2.2. Micro-structural analysis

The determination of phase composition for samples was detected by an X-ray diffractometer (D8 Focus Bruker) with Cu Kα (λ = 1.5406 Å) radiation at 40 kV and 30 mA. Surface morphologies were characterized using a field emission scanning electron microscopy (FE-SEM, Philips/S-4800) equipped with the EDAX analyzer. The mechanical behaviors of samples were measured by NHT Nanoindentation tester with a Berkovich indentor, which manufactured by CSEM Instruments with the load and displacement resolutions of 10 mN and 1 nm, respectively. Results of Hardness and elastic modulus were determined using the classical Oliver-Pharr method [21]. In addition to the dry tribological tests without lubricated conditions, it was placed into a ball-on-disc tribometer (HT-1000) under different heating temperatures in dry air. GCr15 ball, which acted as the pin, was attached onto the specimen's surface. The testing samples used as the disc were tested against GCr15 bearing balls under a loading force of 4.9 N. For distinguishing the wear behaviors from different temperatures, the sliding tests were carried out at room temperature (RT, 25 °C), 300, 400 and 500 °C, respectively. Each test was performed for a period of 15 min, and its coefficient of friction was spontaneously measured from wearing tests. Its specific wear rate was estimated using the equation of $W = V/(FS)$, here W represent the specific wear rate, V is the volume of worn material, F is the normal load and S is the sliding distance.

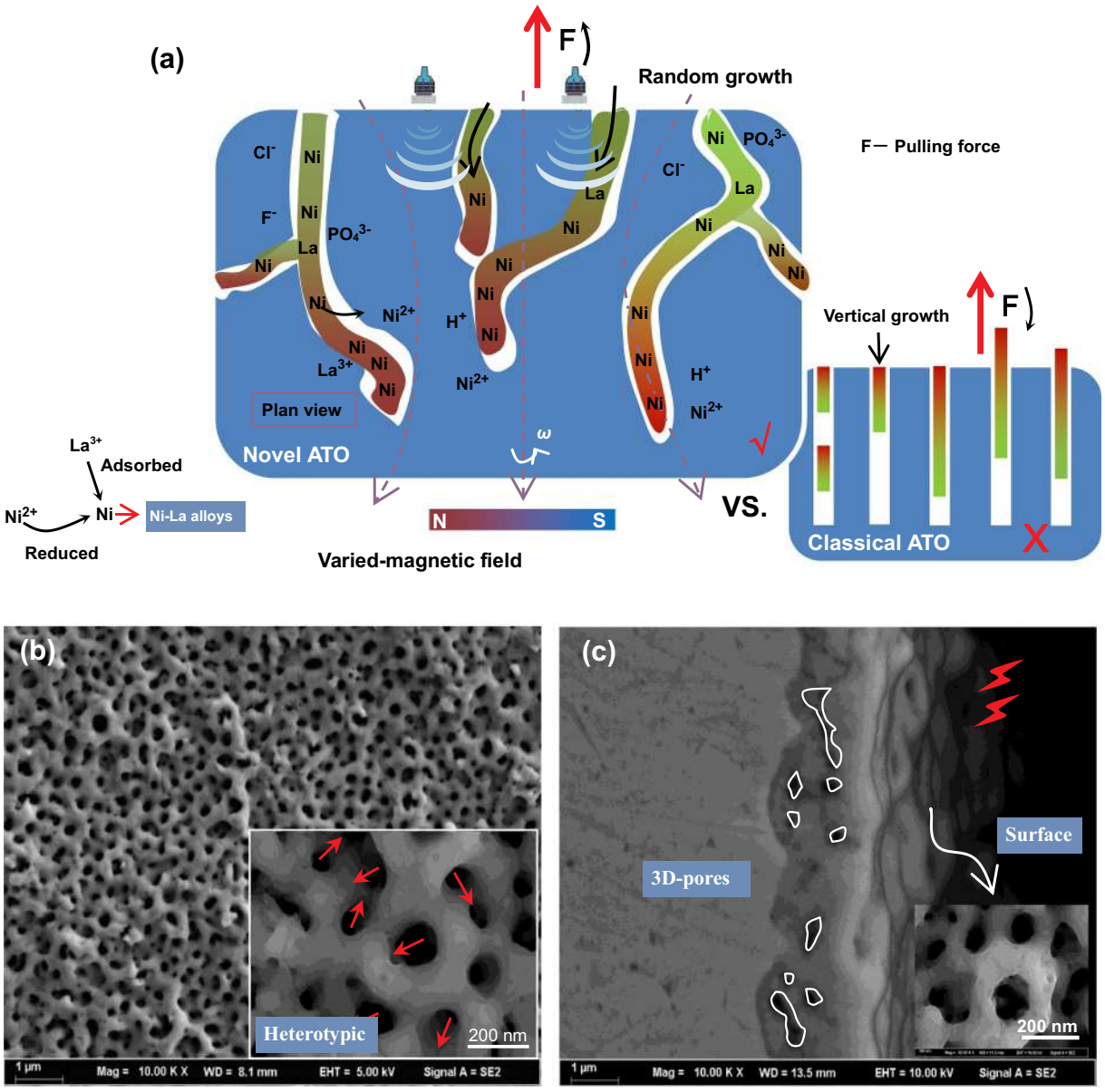

Fig. 1. Schematic description of (a) the magnetic-assisted electroplating processes, and FE-SEM images of (b) a 3D-heterotypic porous surface and (c) the cross-sectional review for ATO pores.

Besides, the cross-sectional profiles of worn tracks were evaluated by a Contour Elite K non-contact optical profilometer.

Electrochemical behaviors of samples were measured in 1 M HCl solution. Electrochemical workstation (AUTOLAB-AUT86742) with a standard three-electrode arrangement was included of a Pt auxiliary electrode and a saturated calomel reference electrode (SCE), and the specimens with an exposed area of 1.0 cm^2 were acted as a working electrode. For details, it was polarized at a scanning rate of 20 mV/min for polarization measurements when the open circuit potential (OCP) remained constant. Electrochemical impedance spectroscopy (EIS) tests were performed over a ranging frequency from 10^5 to 10^{-2} Hz, and its fitting impedance was interpreted based on an electrical equivalent circuit (EEC) via. ZSimpWin software. All the spectroscopy curves were recorded at the respective OCPs using a sinusoidal perturbation signal under an amplitude of 10 mV. After being immersed into 1 M HCl solution for a 5-day time exposed to air, the XRD analysis was determined for detecting their corrosive products. To be clear, above tests were repeated three times to ensure the reproducibility of our results.

3. Results and discussion

3.1. Structural design for Ni—Ti bonding interfaces

In order to improve interfacial bonding strength between Ti substrate and the as-deposited Ni coatings, the as-received ATO porous surface with a 3D-open reticular structure was selected as templates to support many adsorbing sites for Ni—P grains, acting as crystal embryo for inducing the following growth of Ni-$LaCl_3$ coatings. Interestingly, the structural design of 3D-heterotypic pores was likely to make an all-round diffusion for Ni^{2+} and La^{3+} ions through ATO nanopores, thereby leading into an approach for pitting growth of Ni crystals. For details, the Pd-reducing crystal sites through sensitizing-activating processes were used to make preferential locations for supporting the nuclei sites for electroless Ni—P growth [22]. Based on the catalytic nucleation sites by electroless Ni—P embryos, the modified surface for Ti substrate through the Pd-reduced atoms and electroless Ni—P traditional film was finally addressed for developing an easy-handing way to the co-deposition of Ni-based composites on Ti surface.

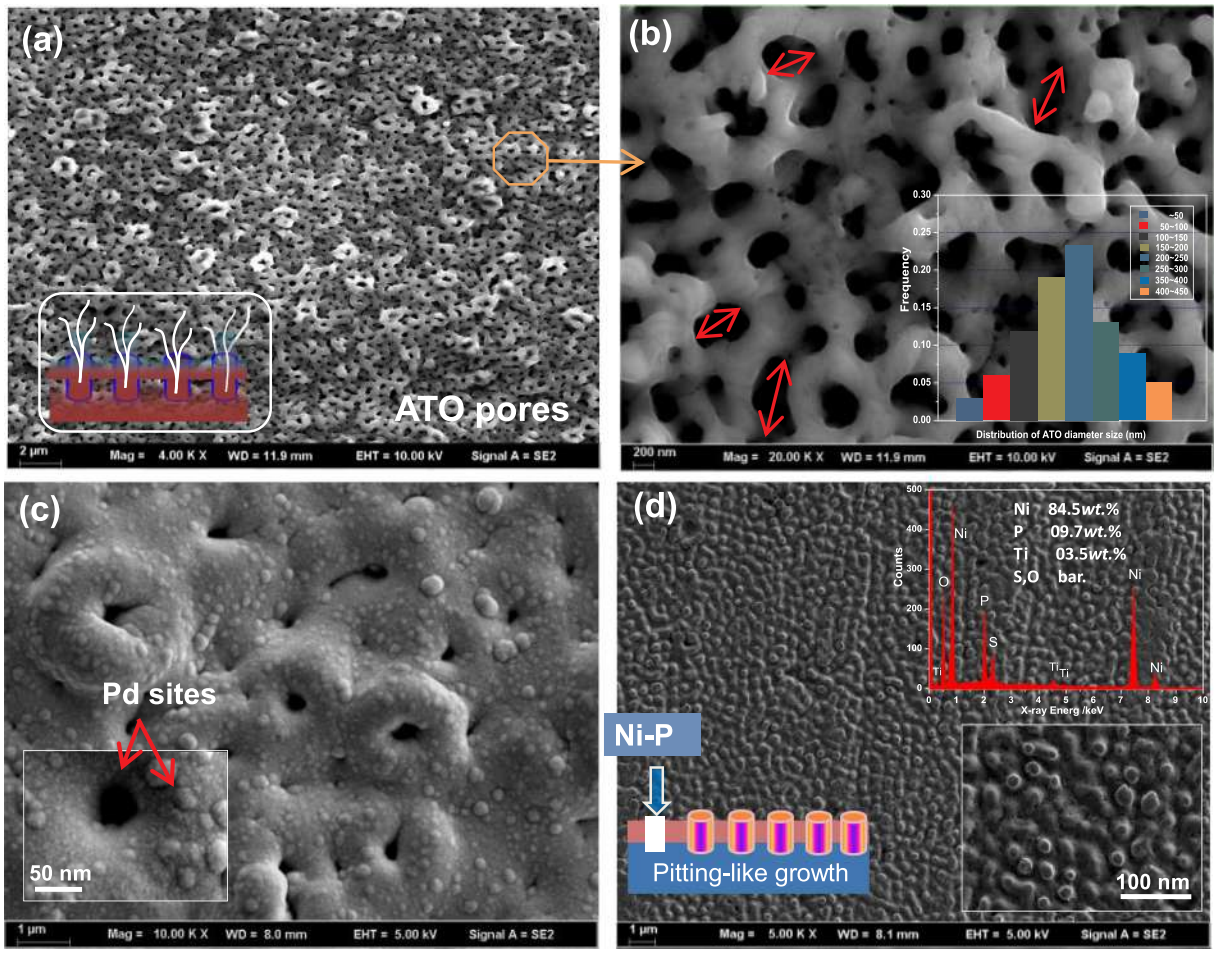

Fig. 2. FE-SEM observations showing (a) nanoporous ATO surface, (b) local amplification for a marked area in (a), (c) Pd-sites decorated nanoporous ATO as catalytic surfaces, and (d) the columnar-like Ni—P growth along pores. Inserted in Fig. 2b is the statistic result of pore-size distribution.

As expected, the sandwich-like structure of Ni-$LaCl_3$/Ni-P/ATO surface was achieved, which was in favor of increasing interfacial adhesion between Ti substrate and its surface films. Among them, electroless Ni—P film was acted as the transitional layer to make a metallic bonding between Ti and Ni (Ni-$LaCl_3$) atoms. Whereafter the catalytic-Pd atoms would support the growing sites for Ni catalysts to make heterogeneous nucleation, as a result of dynamic crystallization. Pd-sites decorated porous ATO surface was expected as an efficient interface for co-depositing Ni-$LaCl_3$ composites with increasing bonding strength. As shown from Fig. 2, the activating processes were followed as: (a) nanoporous ATO surface by anodizing at DC 180 V in H_3PO_4 and H_2SO_4 mixed acids; (b) local amplification for a marked area in (a); (c) Pd-sites decorated ATO as a catalytic surface to induce more nucleation sites ($Sn^{2+} + Pd^{2+} \rightleftharpoons Sn^{4+} + Pd$), and (d) the columnar-like Ni—P growth along the as-anodized pores. Finally, the Ni-$LaCl_3$/Ni-P/ATO sandwich structure was available, thereby achieving great improvements of interfacial bonding strength.

In order to enhance the chemical activities of ATO surface, the H_3PO_4 was used as a typical of activating agents in anodizing solution, which was in consideration of chemical reactions between Ti and H_3PO_4 solution. For details, the Ti—O oxides formed on Ti substrate was removed and further activated as long as it was placed into H_3PO_4 or HCl solution, thus leading into some Ti^+ or Ti^{2+} ions to make bonding actions with PO_4^{3+} or OH^-. While the co-existing H^+ and Ti^+/Ti^{2+} ions were provided with a similar electronegativity and chemical structure, so the H^+ in H_3PO_4 was likely to be partly replaced by Ti^+ or Ti^{2+} ions, thus forming the chemical bond of Ti-PO_4 and then creating the bonding between Ti substrate and surface films in the form of $Ti_3(PO_4)_2{\cdot}4H_2O$ [23]. Besides it was inevitable to occur water electrolysis under a high voltage of 180 V, namely $H_2O \rightleftharpoons H^+ + OH^-$. The existing OH^- was likely to bond with Ti^+ ions and then from the activated surface in the form of active Ti—OH bonds. The active Ti—OH bonds was expected as a chemical bonding bridge, and make the following P═O bonds to be replaced by the P═Ni building-up reactions. For details of activating processes of active $Ti_3(PO_4)_2$ or P═Ni instead of Ti—O chemical bonds, it was schematically illustrated in Fig. 3.

Fig. 4a depicts the cross-sectional SEM image for bonding interfaces between Ti substrate and electroless Ni—P films. Fig. 4b-c exhibits EDS maps of elemental distributions for Ni, Ti and P. The as-anodized ATO template with nanopores surface were served as pitting holes to guild the Ni—P crystals growth into pores, as a result of high bonding strength by means of pitting growth pattern. As expected, the well bonding interface was probably due to the structural design of Pd-reduced atoms to be acted as nucleation sites for electroless Ni—P film, having the bridge-pricking effects. And in accordance with our previous description, small Ni—P crystals formed into ATO nanopores would be expected as growing centers to refine the subsequent Ni-$LaCl_3$ coatings. In view of this, it exhibited higher compactness of Ni-$LaCl_3$ deposits with limited stresses from the Watts-Nickel electrolyte, thereby resulting in a reconstruction of the gradient transition in chemical composition (e.g., Ni—P, Ni-$LaCl_3$).

For experimental results, as depicted in Fig. 5, nanoporous ATO surface was adsorbed by Pd-reduced catalytic sites, Pd-sites decorated porous ATO surface as an efficient interface for co-depositing Ni—P embryos, and then followed by Ni-$LaCl_3$ films onto the activated Ni—P surface, as a result of an increasing of bonding link for Ti—Ni interfaces.

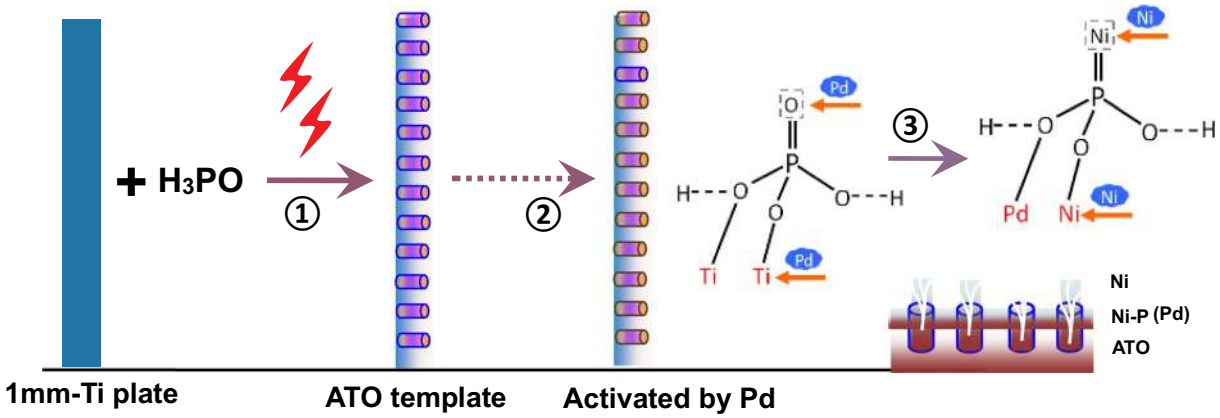

Fig. 3. Schematic illustration of H_3PO_4 activating treatments of the as-anodized ATO surface to form Ni═P chemical bonds instead of Ti—O oxides.

Fig. 5a shows the honeycomb-like ATO surface that anodized from the H_3PO_4-containing acids to support much adsorption space for the following Ni—P embryos. In Fig. 5b, the pitting growth of Ni—P grains along ATO nanopores was indicative of the guiding role for columnar-like crystal growth. And in Figs. 5c and d, the preferential growth of Ni—P crystals were acted as embryos for inducing the Ni-$LaCl_3$ deposits, thus resulting in co-existence of elliptical Ni grains and denser Ni-$LaCl_3$ films with a leaf-like surface by adding of $LaCl_3$ addition into Watts-Ni bath. For details of chemical analysis, please refer to our previous studies in Refs. [17, 20].

3.2. Surface features of Ni-$LaCl_3$ coatings

Fig. 6 exhibits FE-SEM images of surface features for Ni deposits with a functional amount of $LaCl_3$ addition ranging from 0 to 2.0 g/L. Under the optimized electroplating conditions, a flat and smooth surface without obvious void defects or cracks was obtained for pure Ni, as depicted in Fig. 6a. With the introduction of $LaCl_3$ addition, as clearly shown in Fig. 6b-c, a leaf-like surface was observed for the Ni-$LaCl_3$ composites with denser structure. This was mainly attributed to the high adsorption for La^{3+} ions adsorbing onto Ni^{2+} ions, forming the Ni $[La(OH)_4]^+$ complexes to affect original law of the three-dimensional crystallization. Well documented that the La^{3+} ions in bath are processed of larger ionic radius and strong adsorption. During the electroplating processes, the existing La^{3+} will make adsorption towards Ni^{2+} crystal embryo, especially along defectives regions (e.g., GBs, micro cracks). Accordingly, a great adsorption of such incorporated La^{3+} ions that used for increasing the electrocrystalline potential was

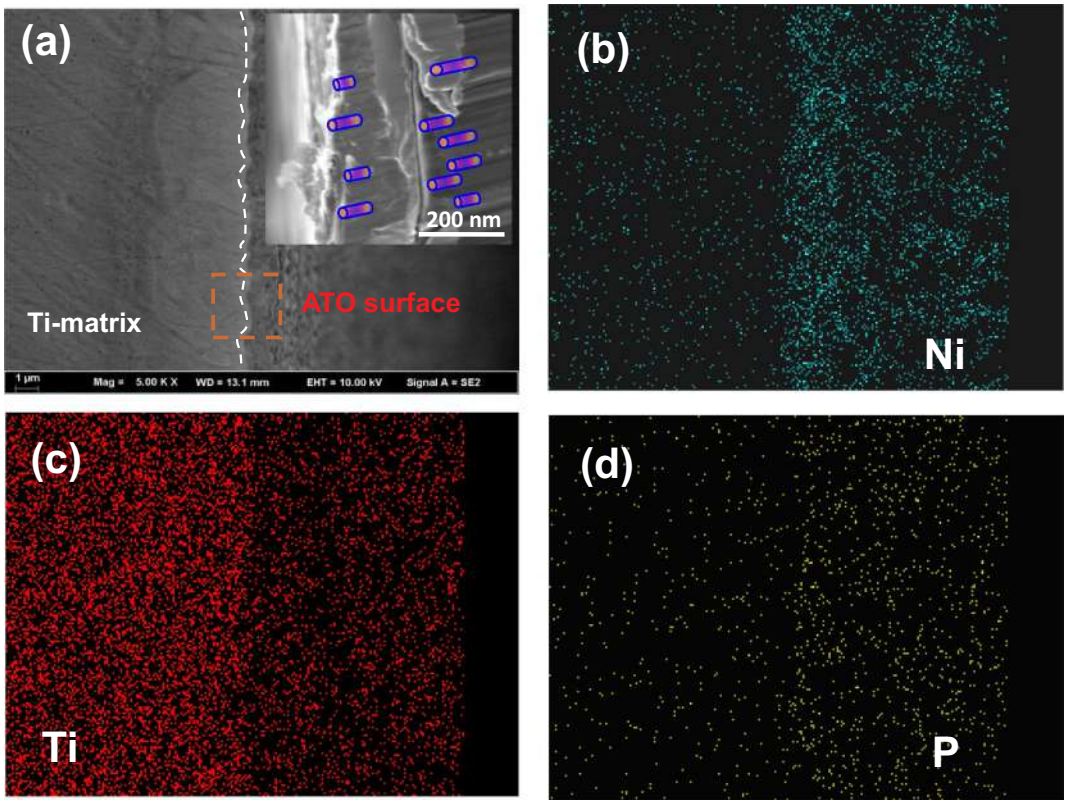

Fig. 4. The cross-sectional FE-SEM image (a) of bonding interfaces for Ni—P growth along ATO pores, and EDS mapping for elemental distributions of (b) Ni, (c) Ti, and (d) P, respectively.

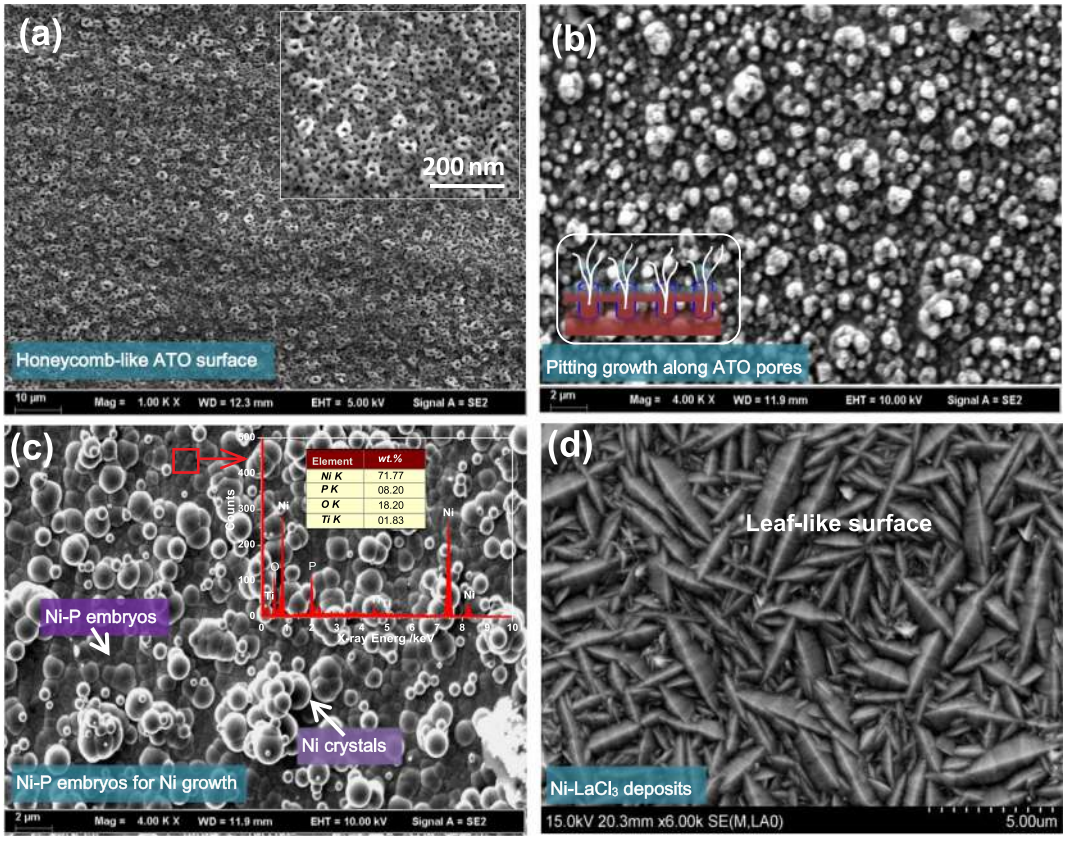

Fig. 5. FE-SEM observations showing (a) well-ordered ATO nanopores by surface anodizing, (b) original Ni—P embryos induced by Pd-sites along pores, (c) the sustained growth of Ni—P film for a traditional layer, and (d) typical surface for Ni-$LaCl_3$ (2.0 g/L) deposits. Inserted in Fig. 5c is the EDS result for a located area.

based on complexing compounds as $Ni[La(OH)_4]^+$, $Ni[B(OH)_4]^+$, et al., thus simulating more re-crystallization of Ni sites by reducing the driving Gibbs free energy for dynamic growth. Similar results were demonstrated by Wang et al. [22] that involved in La^{3+} ions to make pinning effects towards GBs defects for self-organized processes.

As detected in Fig. 6d, it was featured as structural modifications, showing the finer-grained embryos in the co-existence within leaf-like grains for Ni-$LaCl_3$ samples. In the alternative case, the adsorption of La^{3+} ions surrounding the electrode/solution interface would effectively inhibit cathodic reduction, increasing the cathodic overpotential to further refine crystal size. Essentially, the generation of nucleation rate became much faster under more negative of cathodic potential. Meanwhile, the existing La^{3+} ions locating on the crystal surface were in favor of completing the activity defective regions, which was favorable for a finer-grained structure with smooth surface. According to EDS results in Fig. 6b, the chemical composition was consisted of 94.54 wt% Ni, 4.43 *wt*% La and 1.03 wt% O for Ni-$LaCl_3$ (2.0 g/L) samples, respectively. While for small La, it was due to great differences in their electrode potential, namely Ni/Ni^{2+} (−0.257 V) and La/La^{3+} (−2.379 V), in which this was hardly to make co-deposition with La^{3+} and Ni^{2+} in composite bath. While it could be driven by such complexing agents of $C_6H_5O_7^{3-}$ and $B(OH)_4^-$ to make adsorption towards Ni^{2+} or cathode surface, as a result of Ni—La alloys.

In order to study the minute quantities of La on modifying surface smoothness of coatings, 3D roughness reconstruction was detected for Ni deposits without and with 2.0 g/L $LaCl_3$ addition, as arranged in Fig. 7a and b. Fig. 7c depicts the contour curve chart for surface roughness of two samples. As expected, it was finally deduced from statistics results using the least-square method, exhibiting a lower surface roughness (R_a) of ~0.17 for the Ni-$LaCl_3$ composites comparing to that of ~0.32 for pure Ni sample.

3.3. Phase determination by XRD analysis

Fig. 8a depicts the X-ray diffraction patterns for specimens with different $LaCl_3$ amounts (0, 0.5, 1.0, and 2.0 g/L). Five peaks that located at 44.6, 52.1, 76.5, 93.0, 98.5° were assigned into Ni (111) (200) (220) (311) and (222) facets of Ni (JCPDS No. 01–1258). According to a standard PDF card, the highest intensity of preferred orientations has changed from the low-index Ni (111) into high-index Ni (200) (311) facets for Ni-$LaCl_3$ composites, revealing an increasing of Gibbs free energy to impact structural stability. As depicted in Fig. 8b, it was evident that the coefficient of crystallographic texture for Ni growth was in the order of Ni (111) (200) > Ni (220) (311) (222) for tested samples, in which this was in direct proportion to the concentration of $LaCl_3$ addition.

With an increasing of $LaCl_3$ addition from 0 to 2.0 g/L, it exhibited a broadening variation of diffraction peaks' integral widths for such preferred directions as Ni (111) (200) (220), appearing a much decreasing of their relative intensity. Meanwhile the peaks' orientation has transformed from Ni (111) to (200) (311) facets, as indicative of great improvements in coating's toughness [20]. Attentively, a lower atomic density was therefore obtained for Ni (111) comparing to that of Ni (200) reflection in the face-centered cubic (FCC) structure, so its surface energy of Ni (200) was higher than that of (111) leading into more crystallization in Ni (111) close-grained plane. Because of the free-existed La^{3+} ions adsorbing onto $Ni[B(OH)_4]^+$ cations, it could interrupted the normal nucleation of Ni crystals during electrocrystallization processes, thereby resulting in diversified orientations like Ni (220) (311) (222) rather than exclusively growth along Ni (220) and (111). However, the peak of La-rich phase was not obviously found in Ni-$LaCl_3$ composites, which was due to their great differences in standard electrode potential, namely Ni/Ni^{2+} (−0.257 V) and La/La^{3+} (−2.379 V), and it was hardly to make the co-deposition with La and Ni

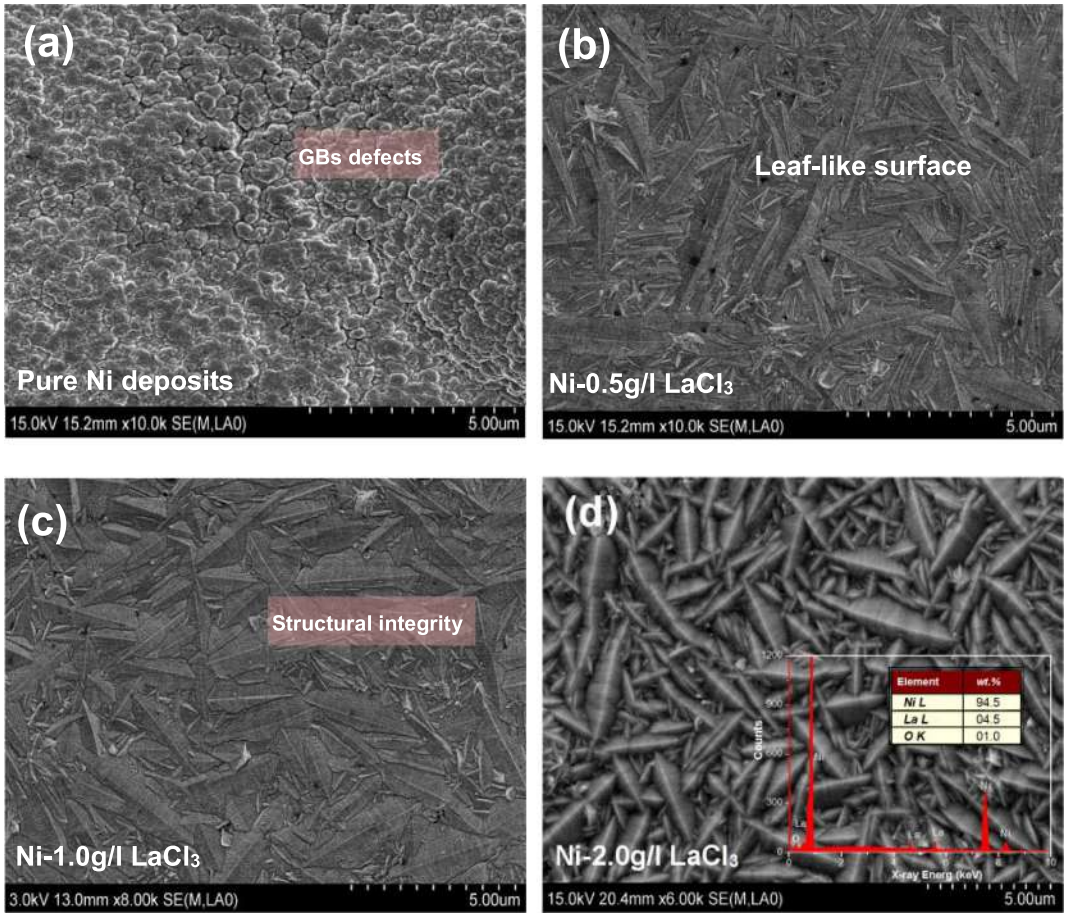

Fig. 6. FE-SEM observations showing surface features for Ni deposits with a functional amount of $LaCl_3$ addition: (a) 0 g/L, (b) 0.5 g/L, (c) 1.0 g/L and (d) 2.0 g/L.

irrespective of having the highest amount of 2.0 g/L $LaCl_3$ addition. From the point of electrochemical view, the La^{3+} ion was hardly to be reduced at the same reduction potential. Nevertheless, the small of free-stated La^{3+} ion was processed of great adsorptive and catalytic activity by means of forming the complexing groups with the free-stated Ni^{+} and OH^{-} ions, namely $Ni[La(OH)_4]^{+}$. For details, two general facts that explicated from above results were summarized as:

(i) The existing La^{3+} ions that adsorbed Ni^{2+} and $Ni[B(OH)_4]^{+}$ cations would be attracted as growing centers to supply location sites for original grains and then make a homogeneous growth.

And more, an increasing overpotential by adding La^{3+} ions in bath was in favor of improving the nucleation ratio of recrystallization, as a result of refined grains. Consequently, the free $La^{3}+$ ions surrounding Ni electrodes could preclude the preferential growth and yield the coarsening growth along a low-index Ni (111) facet. Since its adsorption onto Ni/Ni^{2+} electrode, it would reduce the hydrogen evolution. Similar results were obtained by Ebrahimi et al. [24] and Jeong et al. [25], which was mainly contributed to the effects of RE additive on both fine-grained strengthening and textural reconstruction.

(ii) As we all know that the La^{3+} ion is featured as a larger ionic radius, namely 0.106 nm as relative to that of 0.069 nm for Ni^{2+}. In this case, the co-existence of La^{3+} is more easily adsorbed on the surface of cathode. As the electroplating started, a large number of Ni^{2+} was readily reduced onto the cathode's surface, but La^{3+} did not participate the reduction reaction due to their inherent differences in standard electrode potentials, namely Ni/Ni^{2+} (−0.257 V) and La/La^{3+} (−2.379 V). While small amount of free-stated La^{3+} ions will prone to be non-spontaneously reduced towards high energy regions (e.g., GBs, embryo tips) based on its high adsorption capacity, leading into the heterogeneous nuclei for Ni—La lamellar inter-growth. Soon afterwards, the number of free Ni^{2+} ions decreased with increasing La^{3+} that accumulated the electric-double layer, in which this would obstruct the supply and reduction number of Ni^{2+} during electroplating processes, leading into the reconstruction of textural changes.

To further compare the effect of $LaCl_3$ addition on crystal growth, the classical Scherrer's equation of $D = 0.89\lambda/(B{\cdot}\cos\theta)$, here λ is X-ray wavelength, B is FWHM of diffraction peak, and θ is the diffraction angle, was employed for estimating the crystallite size of Ni grains. According to the XRD line-boarding patterns along the four predominated directions of Ni (111), (200), (220) and (311) facets, a finer-grained size of ~185 nm was achieved for Ni grains in Ni specimens with 2.0 g/L $LaCl_3$ addition, followed by 1.0, 0.5, and pure Ni deposits. As a result, the crystal size of pure Ni was ~250 nm, while the extrapolated size of $LaCl_3$-modified Ni crystals was ~180 nm, in which this value was consistent with above observations (Fig. 6). With respect to the refinement of grain size by $LaCl_3$ addition, it was not only favorable for modifying the mechanical properties of Ni-$LaCl_3$ coatings, but increased its corrosion resistance. In view of this, it provided to a broad new class of RE-rich Ni composites with structural integrity to further extend their use in a variety of industrial applications [26,27].

3.4. Surface toughness by Nanoindentation tests

For simplify, subsequent sections were divided into two typical samples, namely pure Ni and Ni-2.0 g/L $LaCl_3$ composites. Two kinds of samples were finally conductive for a comparative study. Fig. 9 depicts two typical loading-unloading curves, to a maximum applied load of 12 mN, which obtained from both pure Ni deposits and Ni-2.0 g/L $LaCl_3$ composites (The similarly of variation tendency for Ni-0.5, −1.0 g/L samples, so it was omitted). For simplicity, the following excerpt was

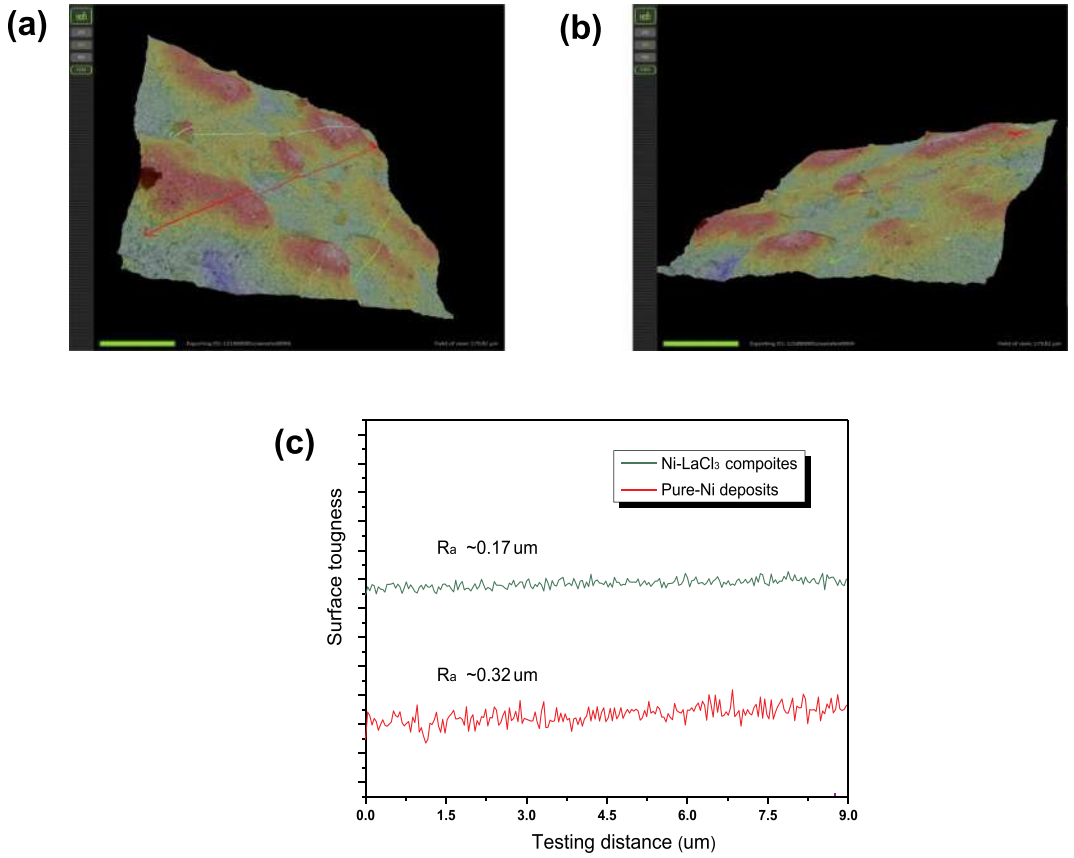

Fig. 7. 3D roughness reconstruction for (a) pure Ni and (b) Ni-$LaCl_3$ (2.0 g/L) composites. Inserted in Fig. 6c is the contour curve for surface roughness.

illustrative of comparing the differences of the as-deposited Ni coatings without and within $LaCl_3$ addition (2.0 g/L). It was clearly evident that the loading curve tested for specimens was smooth and continuous, indicating no abrupt cracking or delamination from Ti surface. As plotted in Fig. 9a and b, the maximum indenter depth for two specimens was less than 150 nm, which was much lower than 10% of the coating's thickness (~5 μm). Thus the reflection of mechanical properties was depended upon the deposits without Ti substrate contribution. According to the load-displacement curves, the total value of mechanical work (W_t) determined by the indenters during loading can be defined as [28]:

$$W_t = \int_0^{h_m} (\alpha_1 \cdot h^{m1})\, dh = \frac{P_m \cdot h_m}{m_1 + 1} \tag{1}$$

here W_t represents the total mechanical work, h_m is the maximum displacement, P_m is the peak load, α_1 and m_1 correspond the fitting parameters for empirical model. The total mechanical work comprised of two components, namely, elastic recovery energy (W_e) and energy dissipation (ΔW). The as-defined value of ΔW, due to plastic deformation, can be estimated from the area according to the loading-unloading curves. On the contrary, the elastic energy for deformation (We) can be determined from the area under the unloading curves. The fraction of elastic recovery work (r_e), referring to the ratio of W_e to W_t, can be given by:

$$r_e = \frac{We}{Wt} = \frac{(m_1 + 1)\cdot(h_m - h_f)}{(m + 1)\cdot h_m} \times 100\% \tag{2}$$

To simplify this formula, the exponents for both the loading and unloading curves are considered equal, namely $(m_1 + 1)/(m + 1) \approx 1$ [29], so the above Eq. (4) can be abbreviated as:

$$r_e \approx \frac{(h_m - h_f)}{h_m} \times 100\% \tag{3}$$

Likewise, the fraction of energy dissipation (rd) can be simplified to:

$$r_d = \left(1 - \frac{W_e}{W_t}\right) \times 100\% = \frac{h_f}{h_m} \times 100\% \tag{4}$$

Regarding the h_f and h_m values that extracted from experimental curves, the r_d values of Ni-$LaCl_3$ composite and pure Ni deposits were 27.2% and 67.0%, in which this was characteristic of much greater resistance to plastic deformation than that of Ni deposits. For details, the extrapolated value, H of hardness for Ni-$LaCl_3$ composite was ~9.62 GPa, which was 2.5 times higher than that of pure Ni (3.75 GPa), as depicted in Fig. 9c. As described above, the textural development of Ni grains from Ni(111) to Ni(200) and (311) was in favor of inhibiting preferred growth to enhance its surface toughness. Besides the experimentally measured Young's modulus, E for the Ni-$LaCl_3$ composite was ~208.3 GPa relative to that of ~98.2 GPa for pure Ni, which was comparable to our previous results in Ref. [15, 20]. In general, hard materials usually show a high resistance to mechanical damages, but fail to surface toughness. Leyland et al. [30] suggested that materials with a high ratio of hardness to Young's modulus (H^3/E^2) exhibit a high wear resistance. According to our experimental comparison, it put forward an effective approach for comparing the sample's toughness based on the relatively ratio of H^3/E^2 for this hard coatings. Impressively, it's therefore deduced that a higher H^3/E^2 ratio of 0.0205 was obtained for Ni-$LaCl_3$ specimens as relative to that of 0.0053 for pure Ni deposits, as indicative of enhanced toughness for the as-deposited Ni sample with$LaCl_3$ addition. As usual, Young's modulus is independent of grain size, but correlates closely with the crystal defects, which means the as-received Ni-$LaCl_3$ composites were provided of a denser structure without cracking defects.

For further measuring fracture toughness, the Vickers and Knoop

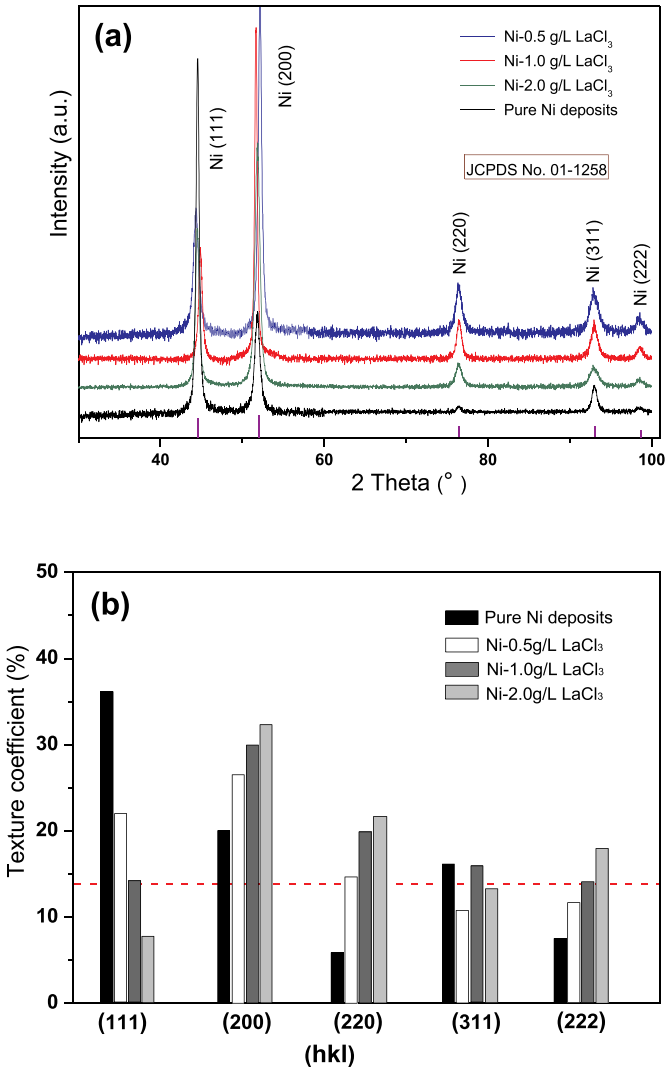

Fig. 8. Typical XRD patterns for Ni deposits with different $LaCl_3$ addition.

indentation techniques were employed. The indentation fracture toughness measured for Ni coatings with and without $LaCl_3$ addition was evaluated using Vickers indentation at different forces ranging from 50 to 500 g. As plotted in Fig. 10, a plan view of OM image for Vickers indentations were observed on the surface of specimens. Here the Ni-$LaCl_3$ composites are processed of higher micro hardness, more than 10 GPa. It must be noted that, though the coating suffered the highest tensile stress, up to a load of 500 g, no obviously micro-cracks were found initiating from the corners of the indents. For details, the annular-like slip-steps that represented the shearing bands were finally observed within the indentation site itself and around the indents, illustrating a continuous edge with no obvious cracks. While it should do not ignorant of local cracks inducing by internal stress. Herein a novel test was determined for surface toughness of samples. Observe carefully how to distinguish between good and bad for coating's toughness, either convergence or local divergence for HV indentations. For the sake of simplification, as loaded at 300 or 500 g, the tested indentation was much larger and deeper for pure Ni relative to that of the Ni-$LaCl_3$ coatings. In general, the tetrahedral feature was featured as a continuously regular indentation for pure Ni deposits, further revealing lower resistance to plastic deformation. While for the case of Ni-$LaCl_3$ composites, a convergence trend with the smaller size was observed for irregular indentations, as indicative of higher resistance to hinder the sliding of dislocations. Without dislocation activity, the plastic

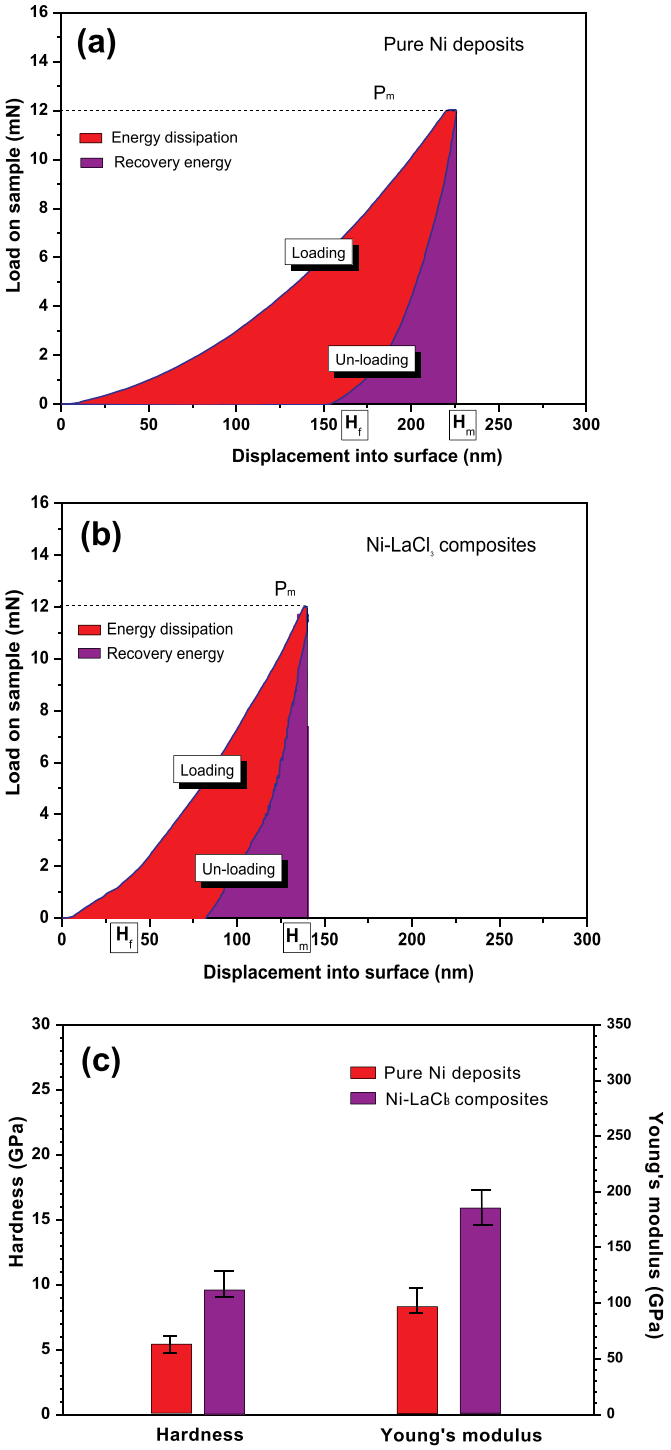

Fig. 9. Load-displacement curves from Nanoindentation tests for Ni deposits without (a) and with (b) 2.0 g/L $LaCl_3$ addition, and (c) Results of hardness and Young's modulus for measured specimens.

deformation of Ni-$LaCl_3$ nanocomposites was analogous, and this deformation was known to be dominated by shear band formation, which were related with a denser structure, together with a textural reconstruction from Ni(111) to Ni(220) (311), as well as the significant REEs by $LaCl_3$ addition adsorbing onto the high-energy defective regions to make pinning effects on inhibiting the sliding movement of grain boundaries (GBs). According to the crystallographic analysis, for fcc-Ni metals, the close-packed Ni(111) surface energy was the lowest among these index surface. Consequently, a threshold value of sliding

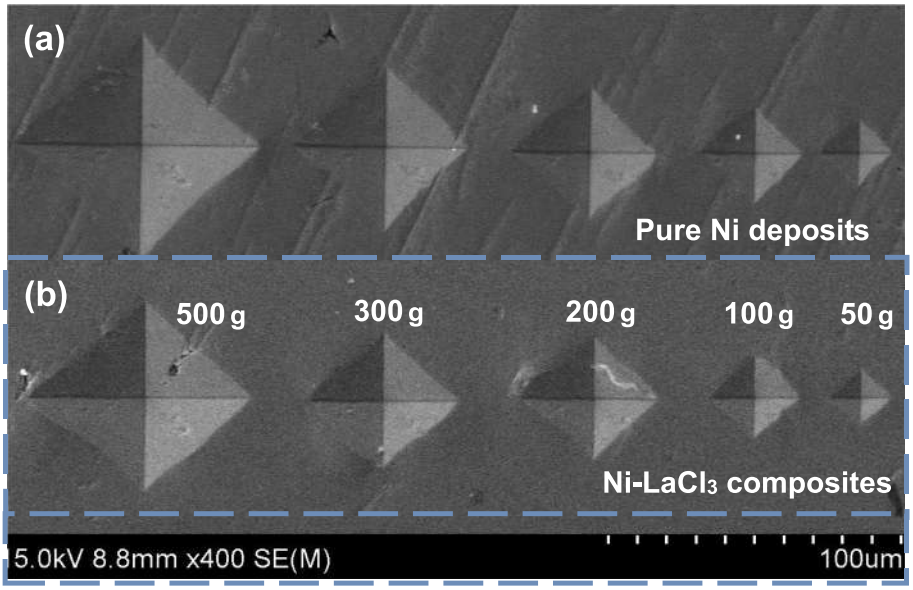

Fig. 10. Optical micrographs (OM) showing Vickers indentation tracks in the surface of Ni deposits without (a) and with (b) 2.0 g/L $LaCl_3$ addition.

activation energy was much lower for Ni(111) plane comparing to those of Ni(200)(220) (311) reflections, which was favorable for increasing the coating's toughness [31,32].

3.5. High-temperature dry wear behaviors

Ni-RE composites that actually used as superalloys in aeroengine components was available for the wear-related applications under high-temperature sliding conditions. Because of dispersion strengthening effects from RE addition, herein heating treatments were carried out for studying the wear behaviors of Ni-$LaCl_3$ composites, implying the La—O disperses on self-lubricating surface of worn tracks. In Fig. 11, the friction coefficients were tested for two samples against GCr15 sphere. In the ball-on-disc test, the GCr15 ball was used as the dis, and the as-prepared sample was served as the pins, in which the sliding tests was carried out in dry air at different heating temperature. As a result, the coefficient of friction for both samples attained a stable value over a narrow range of values during the initial running-in stage, whereas for pure Ni sample it was unstable and signified the worn oscillations over a wider range. Finally, the stable values of friction coefficient increased with increasing temperature from room temperature (RT, 25 °C) to 500 °C, probably due to the co-existence of brittle Ni—O oxides to reduce the resistance to the extrusion and abrasion on the tested samples against GCr15 balls under the dry conditions. As tested at elevated temperatures ranging from room temperature to 500 °C, the coefficient of friction for Ni-$LaCl_3$ sample was the ready-state, only varying in a narrow range from 0.2 to 0.3, which was lower than that of pure Ni sample increasing from 0.4 to 0.6. The lower friction, in return, was contributed to the overall low wear rate. For reasons, the $LaCl_3$ addition were in favor of improvements of surface toughness by means of recombination of textural growth, as well as to modify the textural reconstruction from the exclusively preferred direction Ni(111) into Ni (220) (311), thus reducing the possibility of spalling cracks induced by loose Ni_2O_3 oxides [33].

As discussed in Section 3.2, the $LaCl_3$ addition into Ni deposits was beneficial for yielding the coarsening growth of Ni grains. Explicitly, the effectiveness of La-rich disperses resulting in a self-lubricating worn surface was projected. So a complete set of sliding tests was presented to disclose the $LaCl_3$ effects on wear behaviors during different healing temperatures. Further evaluation of worn tracks was based on SEM observations. As depicted from Fig. 12(a, c, e, g), the severely deeper abrasive grooves were shown for pure Ni sample at RT, 300, 400 and 500 °C, respectively. Inserts are the enlarged images and EDS analysis for worn surfaces, as indicative of different wear mechanisms for two typical samples. The worn products was included of Ni, Cr, Fe and La for Ni-$LaCl_3$ composites, in which a small amount of La was dispersed from GBs regions, and Cr, Fe were from GCr15 balls. In general, the existence of shallower grooves was related with the abrasive La-rich worn products to be acted as solid lubricants and also make the self-repairing effects by completing surface defects [34]. According to the worn characteristics of tested samples, a deeper ploughing friction occurred at de-bonding surface during a short-term heating at 400 °C for pure Ni. While for Ni-$LaCl_3$ composites, a complex model was validated for explaining that a thick La-rich oxide transfer layer over the wear scars, pulling out along a localized region, and partially fueling into the small worn debris, as apparent in Fig. 12 (b, d, f, h), suggesting a typical of narrower and smooth worn tracks for Ni-$LaCl_3$ specimens, which accompanied by some slight abrasion. For details, it was featured as trivial ploughs or scratches, indicating a metallic adhesion without much residuals piled up at the edge of scratch grooves. As a result, the wear mechanisms of Ni-$LaCl_3$ specimens were extended from the severely abrasive or de-lamination wear (pure Ni) into a slightly adhesive wear, and its worn surfaces were therefore governed by a combination of plough friction, abrasive and slight adhesive [35,36].

The specific wear rate was calculated as a measure of the wear resistance for tested samples. For detail, the wear losses (V) was employed using weighing method after the tests of wear tracks depth profiles were completed from the Alpha-Step IQ profilometer. As usual, wear rate (W) was estimated using $W = V/(S \times L)$, here S is the sliding distance and L is the applied load. The specific wear rates were tested under a fixed sliding time of 15 min. For a comparative study, the specific wear rates of two typical samples against GCr15 balls were conducted under different temperature (e.g., RT, 300, 400, and 500 °C). Ultimately, the specific wear rates of Ni deposits (500 °C) was $\sim 10^{-5}$ mm^3/Nm and appreciably increased with increasing the sliding temperature. While for the Ni-$LaCl_3$ sample, its specific wear rates were reduced by about one order of magnitude, showing independent with sliding temperature. Objectively, above results were in good agreement with SEM observations for worn tracks, highlighting the La-rich precipitations formed on worn surface to modify their worn mechanisms. The frictional surfaces can be directly correlated to its surface behavior that extended from fatigue cracks or abrasive grooves to the slight plastic deformations. In theory, the worn surface of Ni sample was likely to leave oxygen vacancies during 400 °C or more, and then occur the

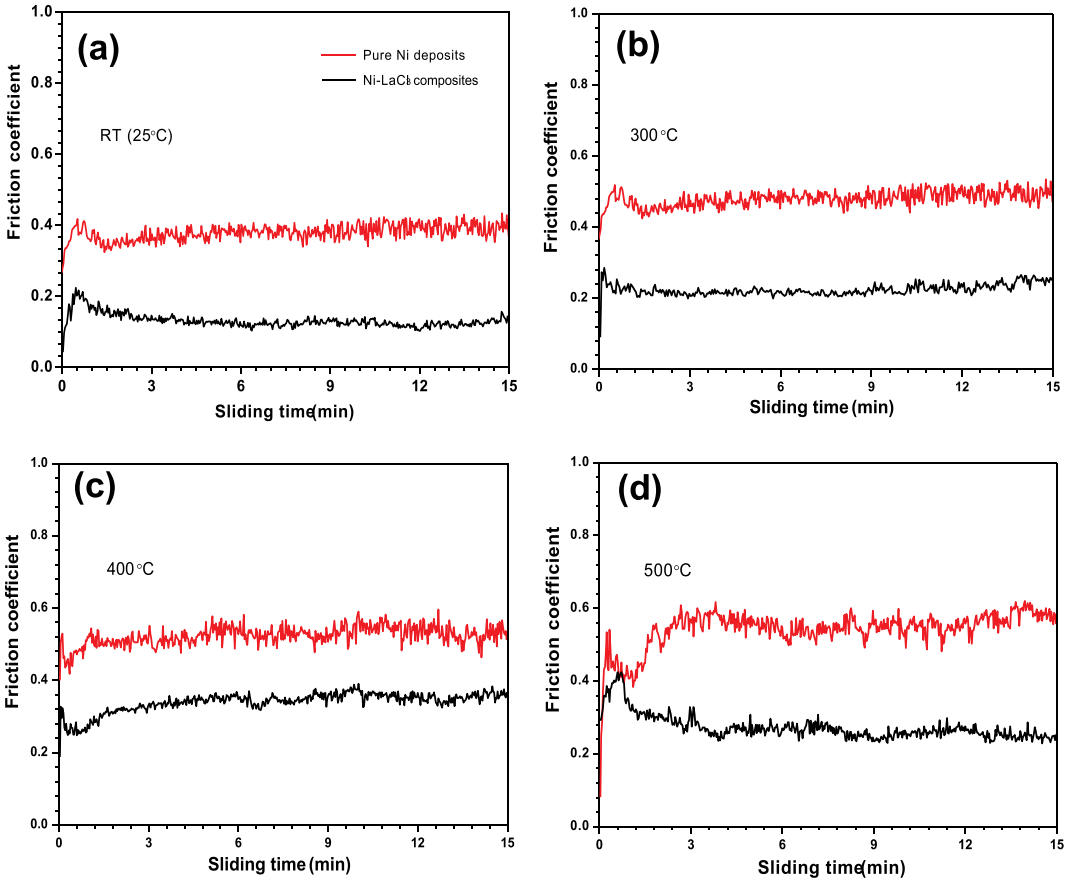

Fig. 11. Variation of friction coefficients vs. time curves for specimens against GCr15 balls under different heating temperatures of (a) room temperature (RT, 25 °C), (b) 300 °C, (c) 400 °C, and (d) 500 °C, respectively.

following oxidation reactions [37]:

For pure Ni sample.

$$Ni + O_2 \rightarrow NiO \quad \text{(major reactions below 400°C)} \tag{5}$$

$$NiO + O_2 \rightarrow Ni_2O_3 \text{(minor reactions above 500°C)} \tag{6}$$

Especially for Ni-$LaCl_3$ composites.

$$La + O_2 \rightarrow La_2O_3 \quad \text{La-rich dispersed debris from Ni-LaCl}_3 \text{ deposits} \tag{7}$$

$$La_2O_3 + NiO \rightarrow NiLa_2O_4 \quad \text{Only for Ni-LaCl}_3 \text{ composites above 500°C} \tag{8}$$

Similar reactions were demonstrated by Zhou et al. [33], illustrating the barrier layers in the form of RE-rich dispersed oxides (e.g., $NiCe_2O_4$) on the surface of Ni-CeO_2 composite coatings. Herein the as-deposited Ni-$LaCl_3$ composites, structurally, contained Ni nano-grains surrounded by segregated La atoms, and its worn surface was covered by La-rich precipitates or as the form of La—O oxides during the dry-sliding heating temperature. As far as the case experiment concerned, the co-existence of NiO and small La_2O_3 oxides was likely to take occurrence of thermal reactions like Eqs. (7), (8). For the $NiLa_2O_4$ spinel phase, it was processed of higher hardness with dispersion strengthening, thus reducing the wear rate of Ni-$LaCl_3$ composites relative to pure Ni. With an increasing of sliding temperature, the wear behaviors of the as-aged Ni-$LaCl_3$ specimens were firstly processed with slightly adhesive or abrasive wear, and then continued with delamination platelets of worn debris, followed by a surface hardening of NiO or Ni matrix. In view of its layer-by-layer assembly of NiO protective layer, the co-existence of the La-rich oxides could be expected as solid lubricants to modify wear behaviors, which formed on worn surfaces to make a self-completing effect on micro flaws, and far from fatigue cracks.

As explained earlier, the Ni-$LaCl_3$ sample showed a smooth worn surface with no evidence of plastic shearing and adhesive characteristics, except a few small pits during worn at 500 °C. For better distributing their differences, the three dimension topography and the cross-sectional profiles of worn tracks was detected for tested samples against GCr15 balls after at a fixed sliding time of 15 min. Figs. 13(a–d) exhibit a plan and cross-sectional view of worn tracks, and Fig. 13e displays the balls indent deeply into surface, showing a large wear scar with the depth of ~40 μm and a width of 2.0 mm for pure Ni. In contrast, the depth and width for Ni-$LaCl_3$ samples were reduced into ~20 μm and 1.2 mm, as indicative of a substantially enhanced wear resistance for Ni deposits within $LaCl_3$ addition [38].

Generally, the elastic modulus is used for evaluating their wear mechanisms, particularly the ratio of hardness to elastic modulus, i.e. H^3/E^2 [39]. Based on above nanoindentation tests (Fig. 9), the H^3/E^2 ratios estimated for the as-received Ni-$LaCl_3$ were about 0.0205, which was much higher than that of 0.0053 for pure Ni (RT, 25 °C). As usual, a higher H^3/E^2 ratio is directly correlated to the better elastic deformation, thereby reducing adhesion damage and modifying the failures of Ni-$LaCl_3$ composites against wear and corrosive damages.

3.6. Electrochemical measurements

3.6.1. Potentiodynamic polarization curves

For ensuring the stability of measured system, the open-circuit potential (E_{ocp}) vs. immersing time curves were tested for both Ni-$LaCl_3$ and pure Ni samples in 1 M HCl solution, as depicted in Fig. 14a. All the OCP curves reached a steady-state condition at a short period, but less time was required for the Ni-$LaCl_3$ sample to attain a stable value, denoting a faster rate of growth for NiO oxides or La-rich passive film.

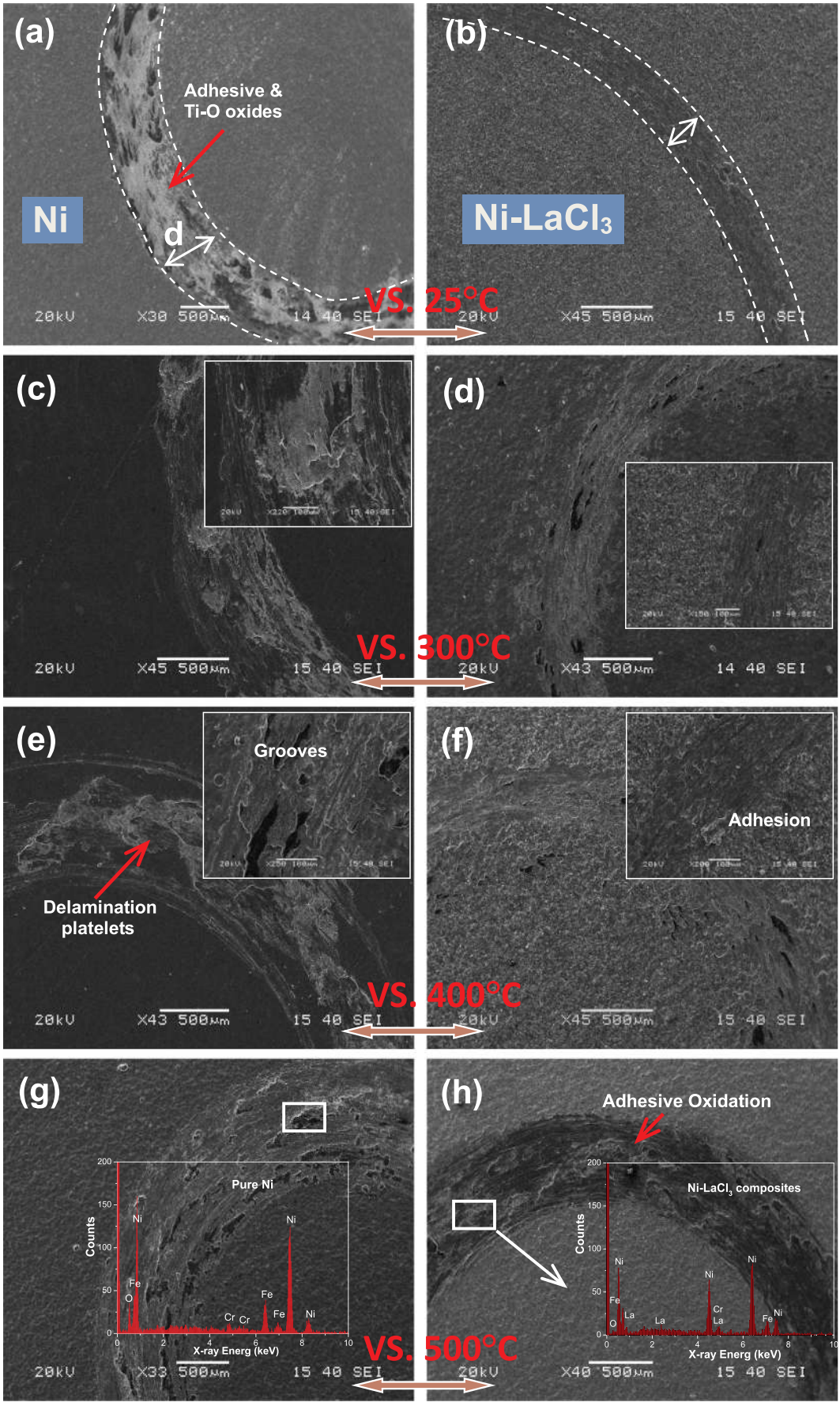

Fig. 12. SEM observations showing the worn tracks of pure Ni (a, c, e, g) and Ni-$LaCl_3$ composites (b, d, f, h) during oxidization at different heating temperature. Inserts are EDS results for worn products of located areas.

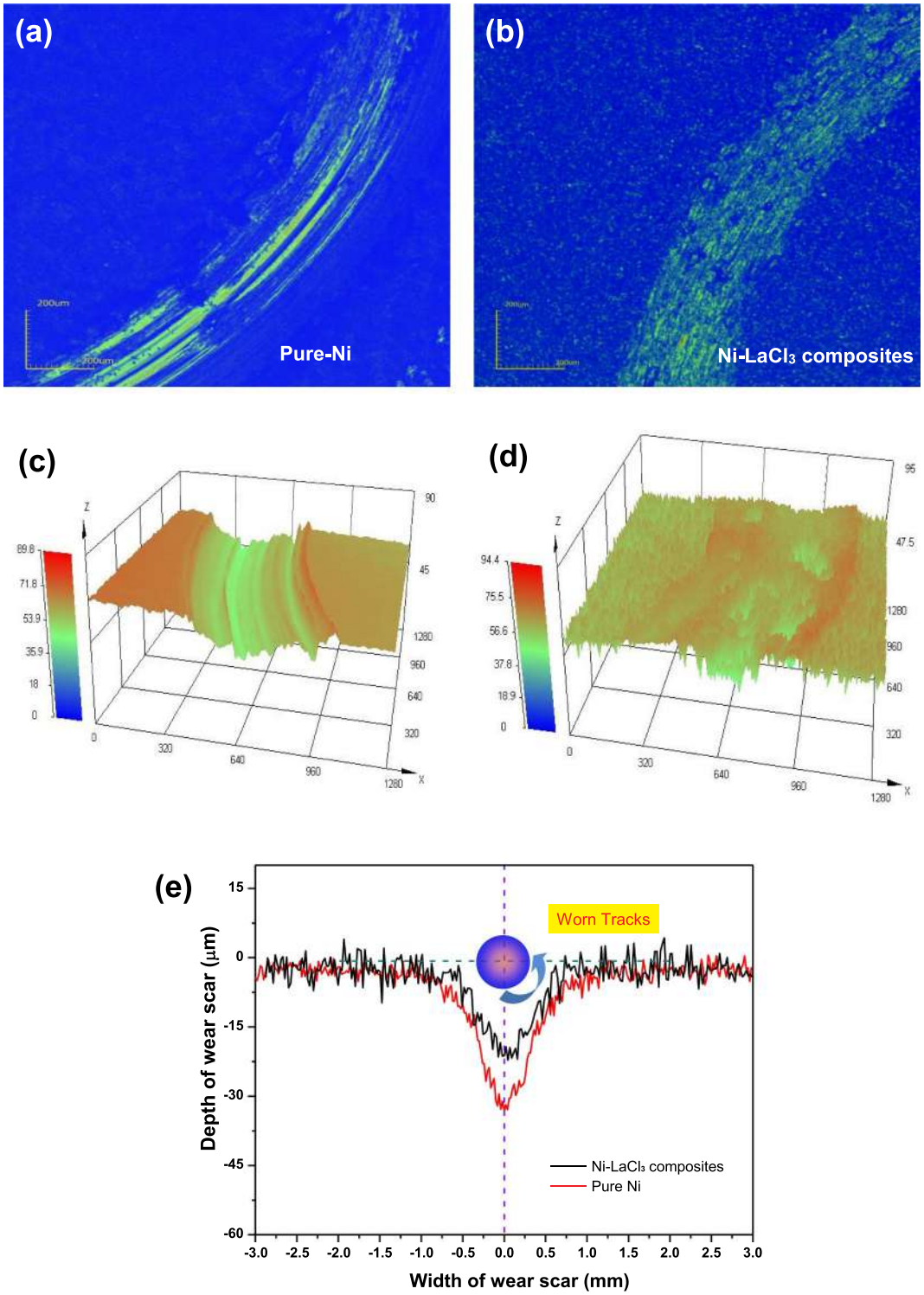

Fig. 13. The three-dimension profiles of worn tracks for Ni deposits without (a, c) and with (b, d) 2.0 g/L $LaCl_3$ addition after being worn at 500 °C, (e) the cross-sectional profiles of worn tracks for tested samples.

Indeed, the E_{ocp} values slightly shifted to be more electropositive of Ni-$LaCl_3$ samples relative to that of pure Ni, and subsequently reach stationary potentials over a period of immersion. As usual, the E_{ocp} value usually reflects the change in the nature of the sample-electrolyte interface as a function of testing time, as well as provides a qualitative analysis for the susceptibility to attack of material surface [40]. According to the Pourbaix diagrams for Ni-H_2O and La-H_2O systems, Ni and La at their respective steady state E_{ocp} are possessed of a passive state, implying an ennobling of their electrochemical behavior. From comparison of the E_{ocp} value at a steady state, it was validated for a more positive potential of $E_{ocp} = -0.19V_{SCE}$ for Ni-$LaCl_3$ composites relative to that of pure Ni sample ($E_{ocp} = -0.25V_{SCE}$), suggesting a compact surface without pining holes or cracks. Thus a La-rich passive film that formed on the corroded surface of Ni-$LaCl_3$ composites had a positive impact on electrochemical corrosion. In particular, it displayed a short-time upward trend at an initial stage of the E_{ocp} vs. time curves

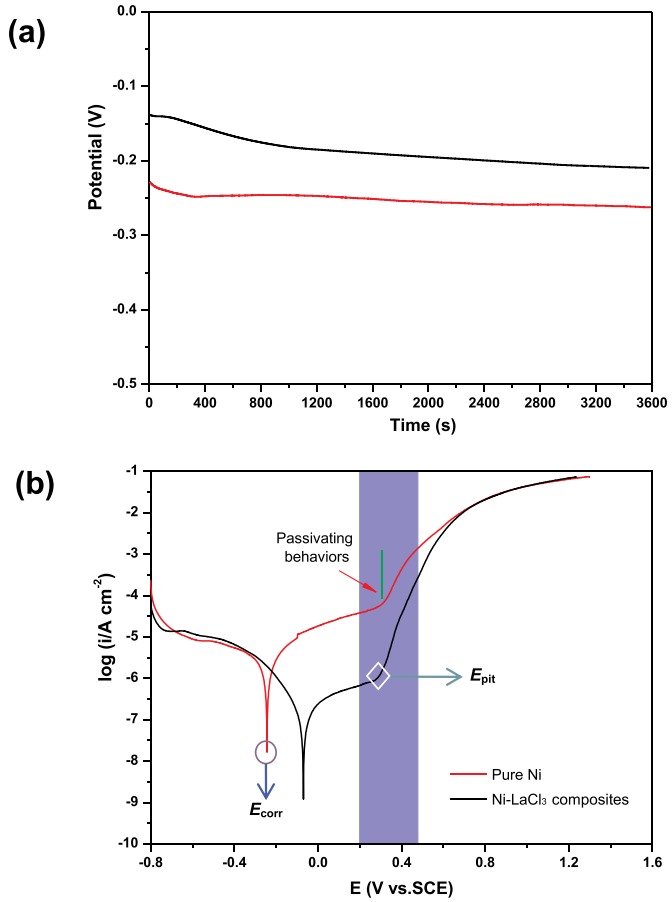

Fig. 14. (a) Typical open circuit potential (E_{OCP}) and (b) potentiodynamic polarization curves (Tafel) for tested samples in 1 M HCl corroding solution.

tested for the Ni-$LaCl_3$ sample, implying the formation of a passive film by precipitation of La-rich conversion films on the corroded surface. Likewise, it was featured as the negative potential, together with an unstable trend at the early stage for pure Ni sample, in which this revealed the anodic dissolution and localized corrosion that occurred at the exposed surface in 1 M HCl solution.

For comparison, the potentiodynamic polarization curves recorded for tested specimens in 1 M HCl solution were polarized from −800 to +1600 mV(vs. SCE) at a scanning rate of 20 mV/min, as plotted in Fig. 14b. According to the Tafel curves, an overlap of anodic polarization curves with an obviously self-passivation behavior was observed, revealing a superior corrosion resistance of samples. In addition, similar of the passive regions was detected, which was probably due to its intrinsically corrosive properties by the Ni or NiO layer instead of La-rich oxides. Besides the characteristics of pitting potential (E_{pit}) were processed with no obviously changes in the periods of stable passivation, indicating the pit incubation and propagation was mainly inhibited by the as-formed NiO layer instead of La-rich oxides for both samples when immersed into 1 M HCl solution. As expected, the anodic and cathodic branches of Tafel curves were similar in the form for both samples, implying a similar reaction was occurred on the surface of tested samples in corroding solution. The electrochemical parameters, including the corrosion potential (E_{corr}), the anodic (β_a) and cathodic (β_c) Tafel slopes, the corrosion current density (i_{corr}) and passive current density (i_{pass}) were derived from polarization curves using Tafel extrapolation, as arranged in Table 2. With respect to the cathodic branch of Tafel curves, the current density increased as the potential moved into a negative direction. Meanwhile the β_c values assigned for two samples were in the range from −131 to −125 mV/decade, which was indicative of the decreasing in the hydrogen transfer activity. The

Table 2
Derived results from potentiodynamic polarization curves of Ni deposits with and without $LaCl_3$ addition in 1 M HCl solution.

Samples	Ni-$LaCl_3$ composites	Pure Ni deposits
E_{corr} (V_{SCE})	–0.13	–0.25
E_{pit} (V_{SCE})	+0.29	+0.30
β_a (mV/decade)	275.32	178.20
$-\beta_c$ (mV/decade)	135.20	205.89
i_{corr} (A cm^{-2})	1.52×10^{-7}	2.82×10^{-6}
i_{pass} (A cm^{-2})	1.18×10^{-4}	2.03×10^{-3}
R_p (Ω cm^2)	2.59×10^{5}	1.54×10^{4}

anodic branch curves of polarization curves were informative of a wider self-passivating region, as predicted, corresponding to better corrosion resistance of Ni deposits due to their structural integrity and its existence of NiO barrier layer. Comparing with pure Ni sample, the polarization curve of Ni-$LaCl_3$ composites was shifted into the right and downwards simultaneously, namely, moving into a more positive potential with a lower-current region. For details, the absolute β_a value was larger than β_c value, particularly for $LaCl_3$-modified Ni coating, implying the control of anodic reactions. These displacements in polarization curves reflected the changes in corrosion reaction's kinetics such as an active anodic dissolution and the reduction of hydrogen ions for measured samples. Generally, the tested surface is nobler if the E_{corr} value is more positive. So the E_{corr} was positively shifted from −0.24 V_{SCE} for pure Ni sample into −0.16 V_{SCE} for Ni-$LaCl_3$ samples. In addition to i_{cor}, it was used for explaining the kinetics of corrosion reactions, which was directly proportional to the corrosion rate. As a result, the i_{corr} of Ni-$LaCl_3$ sample was two one orders of magnitude lower than that of pure Ni, implying a lower rate of corrosive reaction for Ni sample with $LaCl_3$ addition. Similarly, the i_{pass} for Ni-$LaCl_3$ sample was lower than that of Ni sample by approximately one order of magnitude, revealing the formation of a La-rich passive film with a higher electrochemical stability. For the polarization resistance (R_p), it was estimated by the classical Stern-Geary linear equation:

$$R_p = \frac{\Delta E}{\Delta I} = \frac{b_a b_c}{2.303(b_a + b_c)} \cdot \frac{1}{i_{corr}} \quad (9)$$

Here E_{corr} is the corrosion potential; i_{corr} is the corrosion current density, and b_c and b_a represent the slopes for both cathodic and anodic processes, respectively.

3.6.2. Electrochemical impedance spectroscopy (EIS)

The AC-impedance (EIS) measurements were used to compare their corrosive behaviors in 1 M HCl aqueous solution, offering a deeper insight into the electrochemical corrosion. As depicted from 15a, the response in Nyquist plane was sharped as a unique capacitive loop with a widely incomplete semicircle over the frequency range examined, as indicative of a similar capacitive behavior expect their diameter size of capacitive loops. In general, the size of a capacitive loop is positively correlated with the characteristics of the charge transfer, passive film effects, and mass transfer in the passive film. Herein the diameter of capacitive loop in Nyquist was much larger for Ni-$LaCl_3$ sample relative to than that for pure Ni, representing a nobler electrochemical behavior. Likewise, the Z_{imag}/Z_{re} ratio tested for Ni-$LaCl_3$ sample was larger, indicating a higher capacitive capacity of the solid/liquid interface for Ni-$LaCl_3$ sample, in which these results were coincided well with above polarization curves. Without $LaCl_3$ addition, pinholes or cracks that originated from void defects and stress relaxation were likely to occur the localized corrosion of Ni sample when immersed into 1 M HCl solution. With an aid of the free-state La^{3+} ions embedded onto Ni deposits, it was inclined to take an effective adsorption onto the corroded surface and thus, leading into a self-repairing effect on corroded surface to reduce the susceptibility of pitting corrosion. As a scientific hypothesis, the existing La^{3+} to form complexing products were available

for reducing the diffusion rate of charge transfer through the adsorption towards the free-stated H^+ and Cl^- ions. In addition to a small amount of La^{3+} ions, it was processed of 4f electron structure so as to make a special bonding between metal ions (Ni^{2+}) and active ion (Cl^-) in the Ni(La-Cl_x) precipitations, thereby inducing the chemical adsorption onto the corroded surfaces [41,42].

The Bode plots, as apparent in Fig. 16b, similar plots were observed for two samples exposed at 1 M HCl corroding solution, which exhibited a larger capacitive arc with the largest phase angle close to ~85° over a wider range of middle frequencies (10^4–10^1 Hz) for Ni-$LaCl_3$ sample. While for pure Ni deposits, it displayed the largest phase angle of ~−80° over a narrow frequency range (10^3–10 Hz). Besides it expressed the log-linear relationship between impedance value (Z) and frequencies (f), which was indicative of a predominantly capacitive response. In addition to the Bode-magnitude plots, especially at high frequencies ranging from 10^4 to 10^5 Hz, it displayed a constant trendy for log|Z| value, corresponding to the electrolyte resistance between the working and reference electrodes. While in the middle and low frequency ranges, the log |Z| varied linearly with log (f) with a gradient close to 1, reflecting the typical characteristic of a capacitive response for passive films. The log |Z| versus log (f) plot for Ni-$LaCl_3$ sample exhibited a linear relationship over a wider frequency range than Ni sample, further revealing that the NiO and La-rich passive film on the surface of Ni-$LaCl_3$ sample was more capacitive than that on the surface of pure Ni sample. Similarly, the low-frequency limit of impedance modulus ($|Z|_{f\to 0}$), which was the sum of polarization resistance, was distinctly bigger for Ni-$LaCl_3$ coatings than that of pure Ni sample, which could further confirm the better protective properties by the formation of La-rich passive film. In general, the Bode-phase plots was characteristic of a broad phase angle plateau over a wide frequency range with a phase angle maximum close to ~85° for two samples. For better fitting EIS data using the ZSimpWin software, a closer examination was carried out. So two inflections were distinguished from the tested spectrum in the Bode-phase angle plots, inferring that two relaxation time constants were in the spectra, that was, one in the high frequency range and the other in the middle-low frequency range. For detail, two time constants were comprised of two kinds of capacitive characteristics, either at the interface of coatings/corrosive solution or at the boundary of coatings/the passive film (denser NiO oxides). As stated above, the co-existence of La-rich corrosive products on the corroded surface was interpreted as a passive layer to reduce localized corrosion, and far from electrochemical dissolution or diffusion behavior by H^+ ions for pure Ni sample as subjected into 1 M HCl solution. Ultimately, an increasing value of absolute impedance was obtained at the low-frequencies (LF) region for Ni-$LaCl_3$ sample as against pure Ni, most probably due to this barrier layer enrich of a La-rich phase to self-repair the corroded surface by reducing void defects, thus leading into the decreasing rate of charge transfer. While at the high-frequencies (HF) range, the impedance value responded to the surface characteristics of corroded area, nor reflecting the intrinsic quality of the passive film. Based on above arguments, two typical of the electrical equivalent circuits (EECs) were employed, as inserted in Fig. 15b, here R_s is the solution resistance, Q_{dl} represents a constant phase element (CPE) corresponding to the capacitance of the electric double layer at HF region, R_{ct} denotes the charge-transfer resistance, the values of Q_{pf} and R_{pf} are the capacitance and resistance occurred at the dense inner passive layer/corroding solution interface happened at LF range, respectively. Considering the effects of deviations from ideal dielectric behavior from the roughness of the defects and heterogeneities of surface layers, so a constant phase-angle element (CPE) was finally introduced to replace an ideal capacitance element for better fitting. Typically, a Z_{CPE} was defined as follows:

$$Z_{CPE} = \frac{1}{Q(j\omega)^n} \tag{10}$$

where Q is the frequency-independent parameter, w is the angular frequency and j is the imaginary unit. The exponent n, ranging from 0.5 to 1, was resulted from the non-uniform distribution by the surface roughness and defects. The simulated EIS results, as arranged in Table 3, were obtained from the fitting procedures based on ZsimpWin software. The fitting quality was evaluated using the statistical method of typical chi-squared (χ^2) tests. The fitting results were basically of the order of 10^{-4}, implying well representative of electrochemical characteristics using the proposed equivalent circuit for tested samples. According to the calculation from the given EIS models, the resistance value, R_{pf} of the passive layer was ~10^5 Ω cm^2, which was about three orders of magnitude higher than the value for the outer layer (R_{ct}) and showed that this layer was dominant in the protection of both tested samples from attack by corrosion. The R_{pf} value of the Ni-$LaCl_3$ sample was two times higher than that of pure Ni sample. More important, its CPE value of Ni-$LaCl_3$ sample was about a quarter of that for pure Ni. Meanwhile the effective capacitance (C_2) value was replaced by CPE (Q_2) values to better fitting the EIS data, which was given by the criteria from Brug et al. [43]:

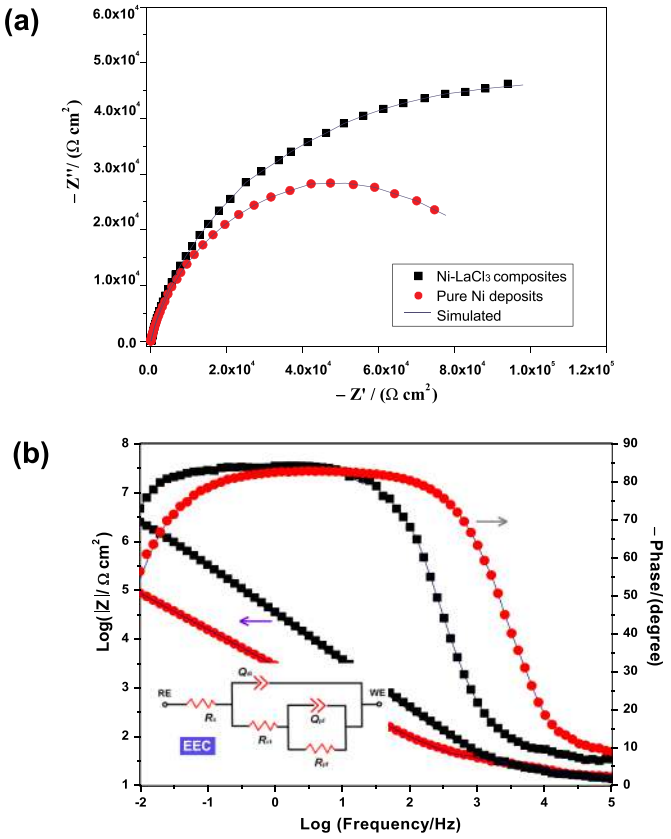

Fig. 15. (a) Nyquist and (b) Bode plots of Ni deposits without and with 2.0 g/L $LaCl_3$ addition in 1 M HCl solution. Symbol: experimental data; line: fitted data.

Table 3
Fitting results of impedance spectra from the proposed equivalent circuit simulation.

Samples	Ni-$LaCl_3$ composites	Pure Ni deposits
R_s (Ω cm^2)	35.81	31.85
Q_{dl} (Ω^{-1} cm^{-2}s^n)	1.71×10^{-6}	1.27×10^{-5}
n_1	0.58	0.69
R_{ct} (Ω cm^2)	275.36	81.25
Q_{pf} (Ω^{-1} cm^{-2} s^n)	6.71×10^{-5}	1.65×10^{-5}
n_2	0.91	0.95
R_{pf} (Ω cm^2)	6.18×10^5	3.08×10^5
C_2 (μF cm^{-2})	1.47	2.25
χ^2	3.51×10^{-4}	6.42×10^{-4}

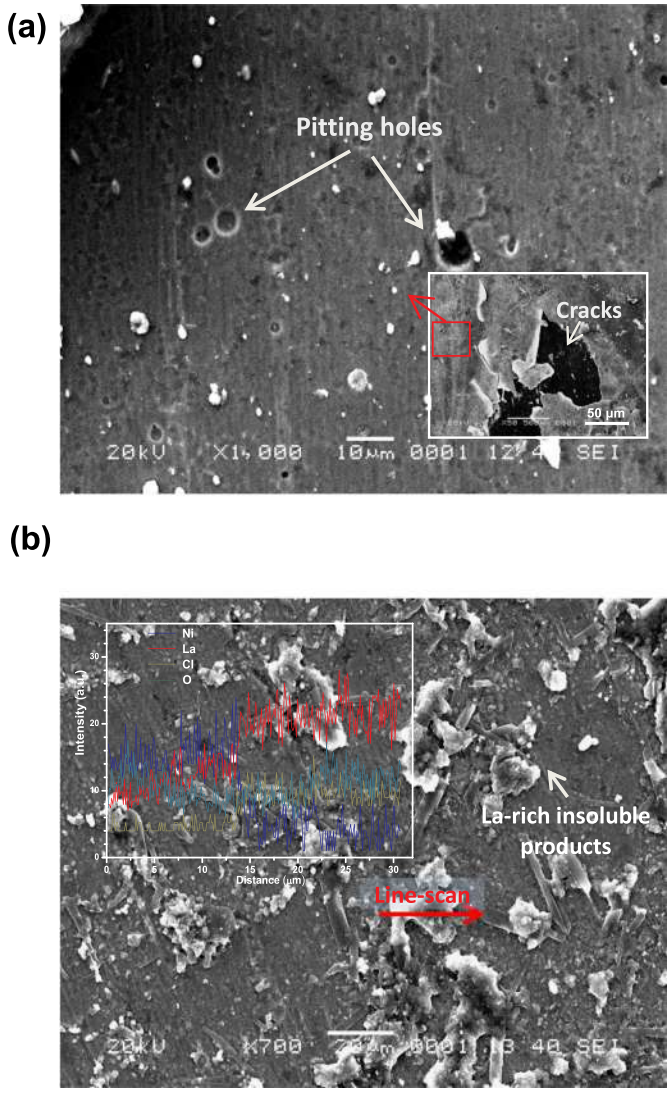

Fig. 16. SEM observations showing the corroded surfaces for (a) pure Ni and (b) Ni-$LaCl_3$ coatings after being immersed into 1 M HCl solution for a 5-week time in air.

$$C_2 = Q_2^{1/n}(R_s^{-1} + R_2^{-1})^{n-1/n} \quad (11)$$

Here the value, C_2, of Ni-$LaCl_3$ composites was smaller than that of pure Ni, which was due to the passive film (e.g. NiO, La-rich) with a lower capacitance and higher resistance. Besides the time constant parameter, defined by $\psi = R_p \times C_p$, was used to evaluate the corrosion rate. Generally, a larger ψ value was obtained for Ni-$LaCl_3$ sample relative to pure Ni, suggesting the passive film (e.g. La-rich products) formed on the corroded surface and make effective in retarding the charge transfer process and ionic dissociation of Ni-$LaCl_3$ sample.

3.6.3. Corrosive inhibition from La-rich products

In terms of corrosive enhancements, the experimental validation of the corroded surfaces was employed for La-containing products. Fig. 16 depicts SEM observations of corroded surfaces for samples after being immersed into 1 M HCl solution for a 5-week time at room temperature. Lots of large pitting holes on the surface were found for pure Ni sample, as shown in plane views. As Inserted in Fig. 16a, it displayed the occurrence of stress corrosion cracking and exfoliation failure, as indicative of poor exfoliation resistance and high residual stress. While for the Ni-$LaCl_3$ sample, Fig. 16b displays a smooth surface without seriously located corrosion, in which insoluble products observed on the corroded surface could be an indirect evidence for uniform corrosion instead of a severely local corrosion for pure Ni sample. Specifically, the EDS-line scan was resulted from the corrosive products of Ni-$LaCl_3$ samples, showing the co-existence of La-rich insoluble products and Ni—O oxides in the Ni-based products. Regarding its high adsorption effects towards pitting defects, this was expected to be the most resistant to uniform corrosion. According to a long-term immersion test in a low concentration of 1 M HCl aqueous solution, a small amount of external O_2 permeated into HCl aqueous solution, followed by pH value gradually increased with decreasing of H^+ in such weak acidic conditions (1 M HCl). Likewise, the possible reactions were as follows:

$$O + 2H_2O + 4e^- \rightarrow 4OH^- \quad (11)$$

$$Ni^{2+} + 2OH^- \rightarrow Ni(OH)_2 \downarrow \text{ or } La^{3+} + 3OH^- \rightarrow La(OH)_3\downarrow \quad (12)$$

Upon a preliminary stage, it was likely to take active dissolution for both samples as:

$$Ni\text{-}2e^- \rightarrow Ni^{2+} \quad \text{(major reactions)} \quad (13)$$

$$H^+ + 2e^- \rightarrow 2[H] \rightarrow H_2\uparrow \quad \text{(major reactions)} \quad (14)$$

For better understanding of inhibition mechanisms, XRD analysis was used to identify the corrosive products with La-rich phase of samples after being immersed into 1 M HCl for 5 days. Fig. 17 displays XRD survey spectrum, including Ni, NiO, $Ni(OH)_2$ and $NiCl_2$ phase, for pure Ni deposits. While for the case of Ni-$LaCl_3$ specimen, it was still composed of Ni, NiO, and $NiCl_2$, together with the co-existing La-rich phase like $LaCl_3$, $La(OH)_3$,etc. During the long-time immersion tests exposed to air, the oxygenation reaction occurred in 1 M HCl weak acid solution, thus leading into an increasing of pH value and gradually tended into neutral solution (pH → 7). So the formation of insoluble products such as $Ni(OH)_2$ and $La(OH)_3$ phase on the corroded surface was likely to sufficiently block pitting pinholes, effectively reducing the diffusing behaviors by H^+ [44–46].

In view of experimental results, as illustrated in Fig. 18, the mechanisms were created for corrosive inhibitions of Ni-$LaCl_3$ deposits, revealing the inhibitions by La^{3+} ions and its La-rich insoluble products. Inserts are the value of contact angle (CA) and SEM images of their corroded surfaces. For details, the Ni-$LaCl_3$ sample was processed of the La-rich conversion film with a larger CA value of ~ 95.2° relative to that of ~ 32.6° for pure Ni. Through being immersed into 1 M HCl solution for a 5-day time, GBs attacks were likely to occur at the corroded surface for pure Ni sample to a large extent. It was mainly ascribed with intrinsical flaws of GBs or micro cracks in the as-deposited Ni coatings (~200 nm crystallites), resulting in the inter-granular

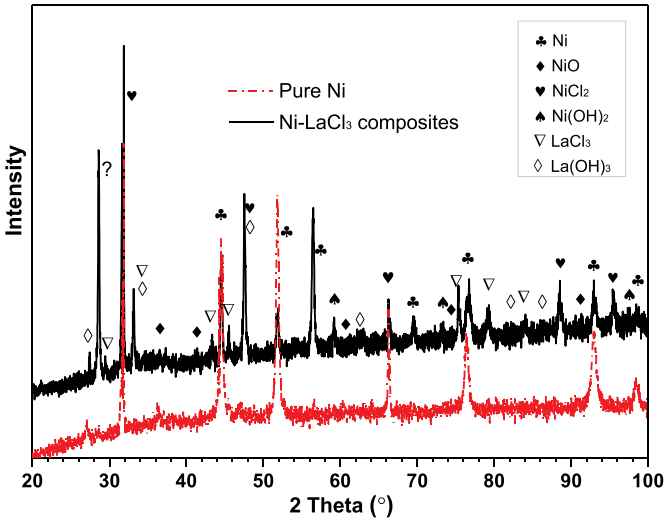

Fig. 17. XRD analysis of corrosive products formed on the corroded surface.

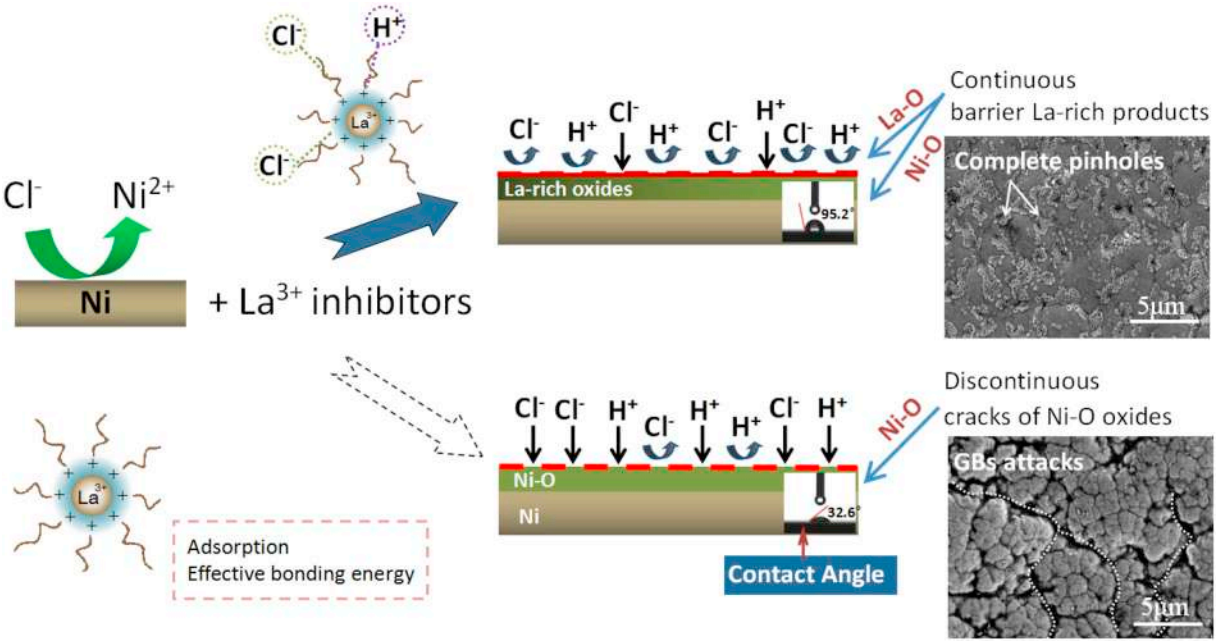

Fig. 18. Schematic of inhibition mechanisms by the free-stated La^{3+} ions and its La-rich insoluble corrosive products. Inserts are the contact angle (CA) and completing of GBs defects by La-rich products.

corrosion or pinholes. This was in consistent with SEM observations for corroded surfaces.

Since the small existing La^{3+} ions ($LaCl_3$) were processed of high adsorption capacity and, thus leading into the precipitations of insoluble complexing products like (Ni, La)$(OH)_5$, $La(OH)_3$, etc. Especially, the La^{3+} ion was typical of a larger size ion radius (La^{3+} 0.136 nm, Ni^{2+} 0.056 nm), which was further intensified the type of chelate complex due to its strong adsorption towards e^- or H^+ [27,47]. As long as the free -stated Cl^- ions were blocked by La^{3+}, the etching damages by Cl^- attacks was reduced by conversion films using the La-rich insoluble products, rather than anodic dissolution (e.g., $NiCl_2$). In light of this, only La^{3+} ions were deemed suitable for their effective on accumulating the adherent La-rich passive films, as a result of the anodic inhibition by means of forming the precipitated (Ni, La)-OH films. And then, such corrosive kinetics like Eqs. (11)-(13) were effectively restrained by reducing the number of e^- or H^+ with the present of free La^{3+} ions. During the long processes of anodic corrosion, the La-rich insoluble products could be defined as hindering agents to reduce the active ions (e.g., H^+, Cl^-), as well as to block the free-stated e^-, and far from the adsorption and diffusion into the pitting region. Indeed, the La-rich insoluble products plugged the pitting holes for effectively decreasing the short-circuit diffusion paths, thus reducing H^+ ions migration and the charge-transfer process.

4. Conclusions

The anodized Ti surface with a 3D-open reticular structure was processed of high adsorption capacity to make an all-round diffusion channels for Ni^{2+} and La^{3+} ions through ATO nanopores, as a result of an increasing interfacial strength between Ti and its surface films. 3D-heterotypic ATO nanopores were well organized with a diameter size of ~300 nm through surface anodizing in H_3PO_4-containing acid solution at DC 180 V. The Ni-$LaCl_3$ composites were processed of a pitting model growth into ATO nanopores. As expected, it was featured as a leaf-like surface with diversified orientations of Ni crystals like Ni (111) (200) (220) (311) for Ni-$LaCl_3$ deposits instead of exclusively growing Ni (111) (200) for pure Ni without $LaCl_3$ addition. Besides similar wear behaviors were tested for two samples without and with 2.0 g/L $LaCl_3$ addition at 200 and 300 °C in air, but differences at 500 °C due to its refinement grains and strengthening from $LaCl_3$ addition. The worn tracks were characteristic of deeper abrasive grooves for pure Ni. For $LaCl_3$-modified Ni sample, while it was featured as a narrower track without spalling behaviors, thus resulting from a combination of plough friction, abrasive and slight adhesive.

For a comparative study, corrosive behaviors of the as-deposited Ni and $LaCl_3$-modified Ni coatings were assessed in 1 M HCl solution, and a superior corrosion resistance was validated for Ni-$LaCl_3$ composites. It's deduced that the self-organized inhibition mechanism was supposed from its La-rich insoluble corrosive products, implying such pitting holes were completed by the precipitated (Ni, La)-OH films for reducing the short-circuit diffusion paths.

Acknowledgements

This work was supported by National Natural Science Foundation of China (No. 51605203), Natural Science Foundation of Jiangsu Province (BK20150467), and Doctoral Scientific Research Foundation of Jiangsu University of Science and Technology (1062921501).

References

[1] X.W. Zhou, Y.F. Shen, A novel method designed for electrodeposition of nano-crystalline Ni coating and its corrosion behaviors in Hank's solution, Appl. Surf. Sci. 324 (2015) 677–690.
[2] W. Teng, X. Li, Q. Zhao, L. Wang, Efficient visible light-induced photoelectrocatalytic degradation of rhodamine B by polyaniline-sensitized TiO_2 nanotube arrays, J. Nanopart. Res. 13 (2011) 6813–6820.
[3] X.L. Shi, L.L. Xu, T.B. Le, Partial oxidation of TiN coating by hydrothermal treatment and ozone treatment to improve its osteoconductivity, Mat. Sci. Eng. C-Mater 59 (2016) 542–548.
[4] K. Hagihara, T. Nakano, Y. Umakoshi, et al., Microstructure and compressive flow stress of directionally solidified ternary Ni_3(Al, Nb) and quaternary Ni_3(Al, Nb, Ti) alloys with duplexphase, Sci. Technol. Adv. Mat. 3 (2002) 193–199.
[5] H. Cho, H.Y. Kim, S. Miyazaki, Fabrication and characterization of Ti–Ni shape memory thin film using Ti/Ni multilayer technique, Sci. Technol. Adv. Mat. 6 (2005) 678–683.
[6] S. Romankov, W. Sha, S.D. Kaloshkin, Fabrication of TiAl coatings by mechanical alloying method, Surf. Coat. Technol. 201 (2006) 3235–3245.
[7] B. Li, Y. Shen, W. Hu, Surface nitriding on Ti–6Al–4V alloy via friction stir processing method under nitrogen atmosphere, Appl. Surf. Sci. 274 (2013) 356–364.
[8] F. Movassagh-Alanagh, A. Abdollah-zadeh, M. Aliofkhazraei, M. Abedi, Improving the wear and corrosion resistance of Ti–6Al–4V alloy by deposition of TiSiN nanocomposite coating with pulsed-DC PACVD, Wear 390–391 (2017) 93–103.

[9] H.X. Liu, B.Y. Tang, L.P. Wang, X.F. Wang, Improvement on surface properties of titanium alloy by plasma immersion ion implantation technique, Rare Metal. Mat. Eng. 34 (2005) 1318–1321.
[10] F. Chen, H. Zhou, C. Chen, Y.J. Xia, Study on the tribological performance of ceramic coatings on titanium alloy surfaces obtained through microarc oxidation, Prog. Org. Coat. 64 (2009) 264–267.
[11] Y.S. Tian, C.Z. Chen, S.T. Li, Research progress on laser surface modification of titanium alloys, Appl. Surf. Sci. 242 (2005) 177–184.
[12] P. Gkomoza, G.S. Lampropoulos, M. Vardavoulias, Microstructural investigation of porous titanium coatings, produced by thermal spraying techniques, using plasma atomization and hydride-dehydride powders, for orthopedic implants, Surf. Coat. Technol. 357 (2019) 947–956.
[13] B. Li, Y.F. Shen, L. Luo, W.Y. Hu, Z.H. Zhang, Surface aluminizing on Ti-6Al-4V alloy via a novel multi-pass friction-stir lap welding method: preparation process, oxidation behavior and interlayer evolution, Mater. Des. 49 (2013) 647–656.
[14] B. Mukherjee, A. Islam, K.K. Pandey, Impermeable CeO_2 overlay for the protection of plasma sprayed YSZ thermal barrier coating from molten sulfate-vanadate salts, Surf. Coat. Technol. 358 (2019) 235–246.
[15] X.W. Zhou, C. Ouyang, Y. Qiao, Y. Shen, Analysis of toughness and strengthening mechanisms for Ni-CeO_2 nanocomposites coated on the activated surface of Ti substrate, Acta Metall. Sin. 53 (2017) 140–152.
[16] U.J. Xue, D. Zhu, F. Zhao, Electrodeposition and mechanical properties of Ni–La_2O_3 nanocomposites, J. Mater. Sci. 39 (2004) 4063–4066.
[17] X.W. Zhou, F. Wu, C. Ouyang, Electroless Ni-P alloys on nanoporous ATO surface of Ti substrate, J. Mater. Sci. 53 (2018) 2812–2829.
[18] C. Vasilescu, P. Drob, E. Vasilescu, I. Demetrescu, D. Ionita, M. Prodan, S.I. Drob, Characterisation and corrosion resistance of the electrodeposited hydroxyapatite and bovine serum albumin/hydroxyapatite films on Ti–6Al–4V–1Zr alloy surface, Corros. Sci. 53 (2011) 992–999.
[19] X.W. Zhou, Y.F. Shen, Surface morphologies, tribological properties, and formation mechanism of the Ni-CeO_2 nanocrystalline coatings on the modified surface of TA2 substrate, Surf. Coat. Technol. 249 (2014) 6–18.
[20] X.W. Zhou, O. Chun, Anodized porous titanium coated with Ni-CeO_2 deposits for enhancing surface toughness and wear resistance, Appl. Surf. Sci. 405 (2017) 476–488.
[21] W.C. Oliver, G.M. Pharr, Measurement of hardness and elastic modulus by instrumented indentation: advances in understanding and refinements to methodology, J. Mater. Res. 19 (2004) 3–20.
[22] X.W. Zhou, C. Ouyang, Wear and corrosive behaviors of electroless Ni-$LaCl_3$ composites on nanoporous ATO surface of Ti substrate, J. Mater. Eng. Perfor. 28 (2019) 2499–2512.
[23] Y.J. Weng, R.X. Hou, G.C. Li, J. Wang, N. Huang, H.Q. Liu, Immobilization of bovine serum albumin on TiO_2 film via chemisorption of H_3PO_4 interface and effects on platelets adhesion, Appl. Surf. Sci. 254 (2008) 2712–2719.
[24] F. Ebrahimi, G.R. Bourne, M.S. Kelly, Mechanical properties of nanocrystalline nickel produced by electrodeposition, Nanostruct. Mater. 11 (1999) 343–350.
[25] D.H. Jeong, F. Gonzalez, G. Palumbo, K.T. Aust, U. Erb, The effect of grain size on the wear properties of electrodeposited nanocrystalline nickel coatings, Scr. Mater. 44 (2001) 493–499.
[26] P. Zhou, W. Li, Y. Li, Fabrication and corrosion performances of pure Ni and Ni-based coatings containing rare earth element Ce and graphene by reverse pulse electrodeposition, J. Electrochem. Soc. 164 (2017) D75–D81.
[27] D. Wang, Y.F. Cheng, H.M. Jin, J.Q. Zhang, J.C. Gao, Influence of $LaCl_3$ addition on microstructure and properties of nickel-electroplating coating, J. Rare Earths 31 (2013) 209–214.
[28] Y.W. Bao, W. Wang, Y.C. Zhou, Investigation of the relationship between elastic modulus and hardness based on depth-sensing indentation measurements, Acta Mater. 52 (2004) 5397–5404.
[29] H. Matsuno, A. Yokoyama, F. Watari, M. Uo, T. Kawasaki, Biocompatibility and osteogenesis of refractory metal implants, titanium, hafnium, niobium, tantalum and rhenium, Biomaterials 22 (2001) 1253–1262.
[30] A. Leyland, A. Matthews, Design criteria for wear-resistant nanostructured and glassy-metal coatings, Surf. Coat. Technol. 177–178 (2004) 317–324.
[31] M.F. Li, N. Li, J.Q. Zhang, C.G. Zhou, Inhibiting effect of Ni-Re interlayer between Ni-Al coating and steel substrate on interdiffusion and carburization, Surf. Coat. Technol. 3237 (2018) 68–74.
[32] Y. Gao, J. Wang, J. Yuan, H. Li, Preparation and magnetic properties of Ni-P-La coating by electroless plating on silicon substrate, Appl. Surf. Sci. 364 (2016) 740–746.
[33] X.W. Zhou, O. Chun, Self-healing effects by the Ce-rich precipitations on completing defective boundaries to manage microstructures and oxidation resistance of Ni-CeO_2 coatings, Surf. Coat. Technol. 315 (2017) 67–79.
[34] N.P. Wasekar, G. Sundararajan, Sliding wear behavior of electrodeposited Ni–W alloy and hard chrome coatings, Wear 342–343 (2015) 340–348.
[35] P. Guo, Oxygen permeability measurements in Ni using H_2/H_2O, CO/CO_2 and Ni/NiO rhines pack atmospheres, Oxid. Met. 83 (2015) 223–235.
[36] X. Lu, X. Feng, Y. Zuo, P. Zhang, C. Zheng, Improvement of protection performance of mg-rich epoxy coating on AZ91D magnesium alloy by DC anodic oxidation, Prog. Org. Coat. 104 (2017) 188–198.
[37] R.Z. Xie, H.Y. Zhang, J.J. Zou, Effect of adding lanthanum (La^{3+}) on surface performance of Ni-P electroless plating coatings on RB400 support anchor rod steel, Int. J. Electrochem. Sci. 11 (2016) 3269–3284.
[38] D.K. Sahoo, R. Mishra, H. Singh, N. Krishnamurthy, Determination of thermodynamic stability of lanthanum chloride hydrates ($LaCl_3{\cdot}xH_2O$) by dynamic transpiration method, J. Alloys Compd. 588 (2014) 578–584.
[39] L.L. Liu, J. Xu, P. Munroe, Z.H. Xie, Microstructure, mechanical and electrochemical properties of in situ synthesized TiC reinforced Ti_5Si_3 nanocomposite coatings on Ti-6Al-4V substrates, Electrochim. Acta 115 (2014) 86–95.
[40] J. Xu, J. Cheng, S. Jiang, P. Munroe, Z.H. Xie, Mechanical and electrochemical properties of a sputter- deposited β-Ta_5Si_3 nanocrystalline coating, J. Alloys Compd. 699 (2017) 1068–1083.
[41] J.H. Song, X.F. Cui, Z. Liu, G. Jin, Z.H. Gao, Advanced microcapsules for self-healing conversion coating on magnesium alloy in $Ce(NO_3)_3$ solution with microcapsules containing $La(NO_3)_3$, Surf. Coat. Technol. 307 (2016) 500–505.
[42] G.H. Wu, H.T. Guo, X.Q. Zeng, W.J. Ding, Effect of $LaCl_3$ on the structure and properties of magnesium alloys, Mater. Sci. Forum 488–489 (2005) 111–114.
[43] G.J. Brug, A.L.G. Van Den Eeden, M. Sluyters-Rehbach, J.H. Sluyters, The analysis of electrode impedances complicated by the presence of a constant phase element, J. Electroanal. Chem. 176 (1984) 275–295.
[44] R.K. Vishnu Prataap, S. Mohan, Electrodeposition of Ni-La_2O_3 composite on AA6061 alloy and its enhanced hardness, corrosion resistance and thermal stability, Surf. Coat. Technol. 324 (2017) 471–477.
[45] A. Aballe, M. Bethencourt, F.J. Botana, M. Marcos, $CeCl_3$ and $LaCl_3$ binary solutions as environment- friendly corrosion inhibitors of AA5083 Al–mg alloy in NaCl solutions, J. Alloys Compd. 323–324 (2001) 855–858.
[46] D. Zhao, J. Sun, L. Zhang, Y. Tan, L. Ji, Corrosion behavior of rare earth cerium based conversion coating on aluminum alloy, J. Rare Earths 28 (2010) 371–374.
[47] G. Shao, X. Qin, H. Wang, T. Jing, M. Yao, Influence of RE element on Ni-P coelectrodeposition process, Mater. Chem. Phys. 80 (2003) 334–338.